An unbinned Fit of H.E.S.S. Sources using the Log-Likelihood Method

Diplomarbeit

von

Kornelia Stycz

Erlangen Centre for Astroparticle Physics
Physikalisches Institut 2
Lehrstuhl für Physik
Friedrich-Alexander-Universität
Erlangen-Nürnberg

1. Gutachter: Prof. Ch. Stegmann
2. Gutachter: Prof. A. Kappes

10.November 2010

Abstract

The High Energy Stereoscopic System (H.E.S.S.) is an array of four imaging atmospheric Cherenkov telescopes. It detects gamma-ray photons in the energy range of 100 GeV to 10 TeV with an angular resolution of $\sim 0.1^\circ$. However, the resolution depends on several factors, for example the energy of the photon and the observation position. In this work, these dependencies were studied in detail with the help of Monte-Carlo Simulations. The obtained parametrization of the point spread function was used to implement an unbinned log-likelihood fit for H.E.S.S. sources. Finally, this fit was applied to two point-sources.

Kurzfassung

Das "High Energy Stereoscopic System" (H.E.S.S.) besteht aus vier abbildenden atmosphärischen Cherenkov-Teleskopen. Es detektiert hochenergetische Gamma-Strahlung in einem Energiebereich von 100 GeV bis 10 TeV. Die Richtungsauflösung einzelner Ereignisse liegt bei etwa 0,1°, allerdings ist sie von verschiedenen Faktoren, wie zum Beispiel der Energie des Teilchens und der Beobachtungsposition, abhaengig. In dieser Arbeit wurden zunaechst die verschiedenen Abhaengigkeiten an Hand von Monte-Carlo Simulationen untersucht. Die Parametrisierung der Auflösungsfunktion wurde genutzt, um einen ungebinnten Log-Likelihood Fit für H.E.S.S.-Quellen zu erstellen. Schliesslich wurde der Fit-Algorithmus auf zwei Punktquellen angewendet.

Contents

1 Introduction

Although astronomy is one of the oldest sciences, it was restricted to the narrow waveband of optical light before the beginning of the last century. With steady progress in physics and technologies, astronomical objects could be observed in other ranges of the electromagnetic spectrum, enabling us to see the universe in a completely new way. Starting with radio astronomy, the lowest energetic radiation, in the 1930's, ultraviolet (UV) and X-ray astronomy succeeded in detecting objects outside the solar system in the second half of the century. Finally, photons with energies >100 GeV could be detected and traced back to a source by the Whipple Observatory in 1989, see [1].

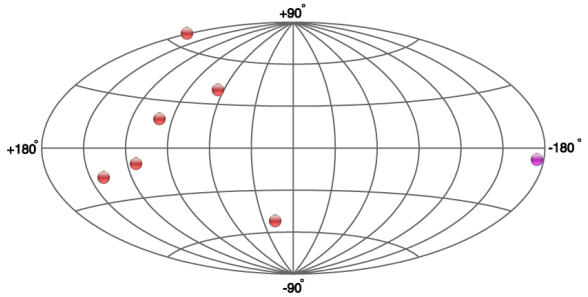

Figure 1.1: *Known sources in the TeV-range at the end of the 1990's in the galactic coordinate system. The pink dot is the Crab Nebula, the first source detected in gamma rays. The red dots are AGNs. Picture generated at [2].*

Unlike the radiation observed in the lower range of the electromagnetic spectrum, these photons, called very high energy (VHE) gamma-rays, can not have gained their energy in thermal processes. One reason for this assumption is the power-law form of their energy spectrum, which does not indicate any characteristic temperature. Moreover, as even the black-body radiation of the hottest astronomical sources does not exceed 10 keV, gamma-rays must be produced by non-thermal acceleration. Consequently, gamma-ray emission characterizes the most powerful processes in the universe like supernovae, pulsar winds or Active Galactic Nuclei (AGN). The two most important acceleration processes are Inverse Compton (IC) scattering and the decay of neutral pions. IC gamma-rays with energies in the TeV-range are generated by multi-TeV electrons interacting with background photon fields like the 2.7 K cosmic microwave background. The decay of π^0-mesons is a consecutive reaction to $pp \longrightarrow \pi^0$, which occurs if two protons with kinetic energies exceeding 0.3 GeV interact. It is still uncertain, what kind of mechanism could accelerate the electrons and protons to that extent, but lots of other high-energy particles hitting the Earth's atmosphere in the form of cosmic rays (CR), give evidence of extreme accelerations. As VHE photons depict these processes, gamma-ray astronomy might provide a hint to the solution of the puzzle. In contrast to most cosmic ray particles, photons can propagate unperturbed through cosmic

magnetic fields and keep their directional information, which makes them suitable messenger particles.

Today, gamma-ray astronomy is well-established as a discipline on its own. In the 1990's, about 10 sources were observed, but a rapid development took place with the operation of several new gamma-ray telescopes like H.E.S.S., MAGIC, and VERITAS, at the beginning of the 21^{st} century. The increase in the number and variety of sources in this short period of time is visualized in Figures 1.1 and 1.2. Nowadays, over 100 sources are known in the TeV-range, some of them were never detected before. Besides, the angular resolution was improved allowing morphological studies of extended objects. As most of them can be observed in other wavebands like radio or X-ray, too, comparisons of the morphologies in different energy ranges became possible. However, the resolution of gamma-ray telescopes is still comparatively low. This work deals with a possible way to augment it by the means of the statistical method of log-likelihood.

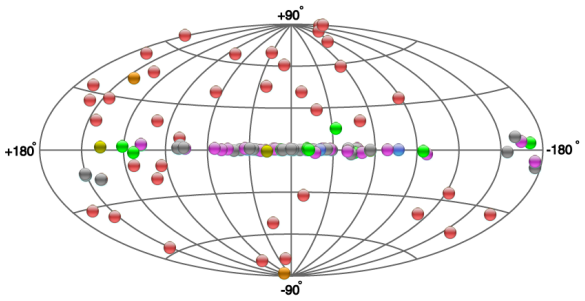

Figure 1.2: *Sources of the TeV gamma-ray sky today in the galactic coordinate system. Red dots mark AGNs, pink ones Pulsar Wind Nebulae (PWN) and green ones are shell-type supernova remnants. The two orange dots are starburst galaxies and the yellow ones are X-ray binaries. Sources depicted in grey are unidentified or do not fit in any of the other categories. Picture generated at [2].*

2 Detection of very high energy gamma-rays

The Earth's atmosphere is not transparent for gamma-rays, making direct observations with terrestrial telescopes impossible. There are two ways to omit this problem, the first one is to observe gamma rays outside the atmosphere in satellite experiments. Since the size and weight of instruments which can be transported to space is limited, the collection areas of the detectors are rather small. This restrains the sensitivity because the low gamma ray flux in the VHE range requires large detection areas.

The other possibility is to use the atmosphere itself as a detector for ground-based observations. The idea is to detect gamma-rays indirectly via secondary particles produced in extensive particle cascades initiated when the gamma-ray interacts with air particles. The particles in the cascade emit Cherenkov radiation in turn, which is ultraviolet/blue light and thus can be seen by optical telescopes. This is the effect used by Imaging Air Cherenkov Telescopes (IACT) like H.E.S.S. Since not only high-energy photons generate particle cascades, but most of the constituents of cosmis rays, a crucial task of IACTs is the discrimination between cascades initiated by the different particle types. The recognition of cascades initiated by protons and other nuclei is most important as they are the main constituent of cosmic rays. In this chapter, all processes needed to understand the principles of gamma-ray detection in the atmosphere will be explained.

2.1 Air shower formation and Cherenkov radiation

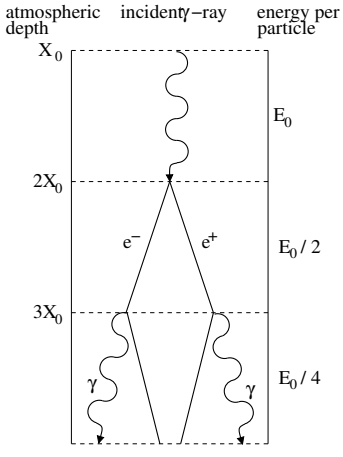

Figure 2.1: *Heitler's model of shower formation. Figure taken from [3]*

When a high-energy photon enters the earth's atmosphere, it interacts with the molecules and atoms in the air, causing a cascade of secondary particles. The development of this so-called electromagnetic air shower can be described as follows: The primary photon produces an electron-positron-pair in the Coulomb-field of a charged atmospheric particle. The electron and positron generate gamma-ray photons via Bremsstrahlung, which, in turn, can lead to subcascades. This process is repeated until the energy of the electrons becomes lower than the critical energy E_c, which is approximately 80 MeV in air - at this point, the ionisation of air molecules dominates over Bremsstrahlung and the production of new photons ceases. The atmospheric depth at which the electron energy drops below E_c is referred to as the shower maximum. It is reached at $\sim 8 - 12\,\mathrm{km}$ above sea level, while the first reaction in the atmosphere typically occurs at $\sim 15 - 20\,\mathrm{km}$.

A simple model for the shower development was introduced by Heitler [4] in 1954. It is based on two assumptions: First, that after one radiation length X_0 each photon creates an electron-positron-pair and distributes its energy equally between both particles. Second, each electron and positron creates one Bremsstrahlung photon with exactly one half of its energy. These processes are visualized in Fig. 2.1 for three radiation lengths. The number of particles N is doubled after one radiation length while their average energy E is halved, resulting in some simple functions of the atmospheric depth X:

$$N(X) = 2^{X/X_0} \tag{2.1}$$

and

$$E(X) = E_0 \cdot 2^{-X/X_0}, \tag{2.2}$$

E_0 being the energy of the primary particle. The maximum number of shower particles scales linearly with E_0,

$$N_{\max} = \frac{E_0}{E_c}, \tag{2.3}$$

and the atmospheric depth of the shower maximum depends logarithmically on it,

$$X_{\max} = X_0 \cdot \frac{\log(E_0/E_c)}{\log(2)}. \tag{2.4}$$

This model may seem too basic, but it features the most important shower characteristics like the exponential increase of the particle number and its dependency on the primary energy.

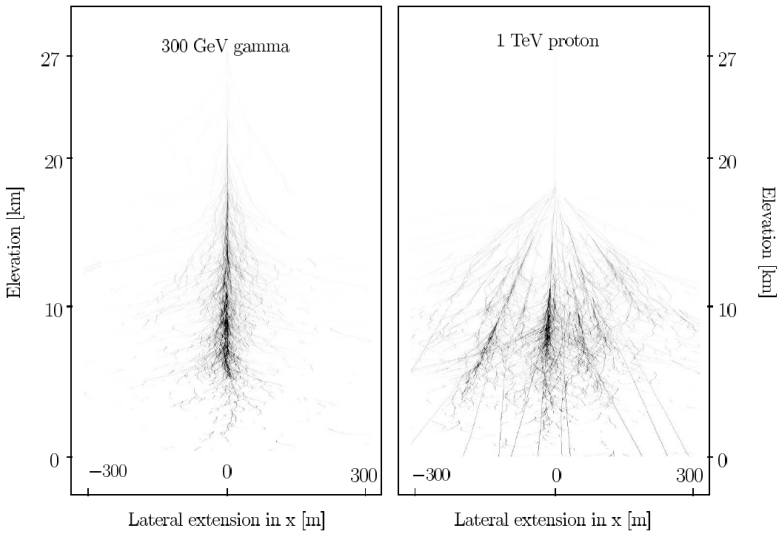

Figure 2.2: *Electromagnetic (left) and hadronic (right) air shower (Figure from [5]).*

As mentioned above, protons and other nuclei initiate particle cascades as well. These are called hadronic air showers and are a main cause of background in ground-based gamma-ray detection. Generally, hadronic showers reach large extensions during their propagation through the atmosphere due to strong interactions which can result in secondary particles with high transverse momentum. On the opposite, electromagnetic showers propagate in a narrow cone which is only slightly broadened by multiple scattering - the difference can clearly be seen in Fig. 2.2.

However, the air shower particles themselves are not detected directly by IACT. What is taken advantage of is the property of fast charged particles to emit Cherenkov light.

Most secondary particles in gamma-ray induced air showers have highly relativistic energies. Their velocities v exceed the local phase velocity of light in air (c/n) with n denoting the refraction index. This is the requirement for the mechanism of Cherenkov radiation which can be described as follows: If a charged particle moves through a medium, the ambient matter is polarized and the induced dipoles emit electromagnetic waves to relax. If the transient particle is comparatively slow, the emission undergoes destructive interference. Particles moving faster than the local speed of light, on the other hand, make the relaxing dipoles interfere in a way that leads to the formation of a wave front (see Fig. 2.3). Analogous to a sonic boom, the shock front forms a cone with an opening angle of

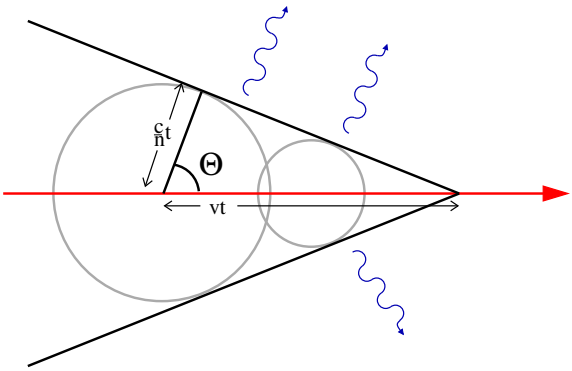

Figure 2.3: *Mechanism of Cherenkov radiation (Figure taken from [3]).*

$$\theta_c = \arccos \frac{1}{n \cdot \beta}, \tag{2.5}$$

where θ_c is being called the Cherenkov angle. As the refractive index n changes according to the density of the atmosphere, both the energy threshold for Cherenkov radiation and the emission angle depend on the altitude. A typical value for the opening angle of the Cherenkov cone is $\sim 1°$.
Due to absorption and scattering processes many Cherenkov photons do not reach the ground, leading to a very faint signal. A primary gamma-ray of 1 TeV energy, for example, illuminates an area with a radius of about 130 m with a photon density of 100 photons/m^2 at 2000 m above sea level, [5]. In addition, a Cherenkov flash has an extremely short lifespan: All the photons of a shower are emitted in $\sim 5 - 20$ns.

2.2 Imaging atmospheric Cherenkov technique

IACTs use the atmosphere as a detector by taking images of Cherenkov light emitted in air showers. As explained in the last section, the Cherenkov emission is very faint and short, therefore IACTs need large light collecting areas to gain as many photons as possible, and fast camera electronics detecting photons on nanosecond time scales. Typically, IACTs consist

of many mirrors focused on one common focal plane, where the camera is situated. The principle of how air showers are depicted in camera images is shown in Fig.3.2.

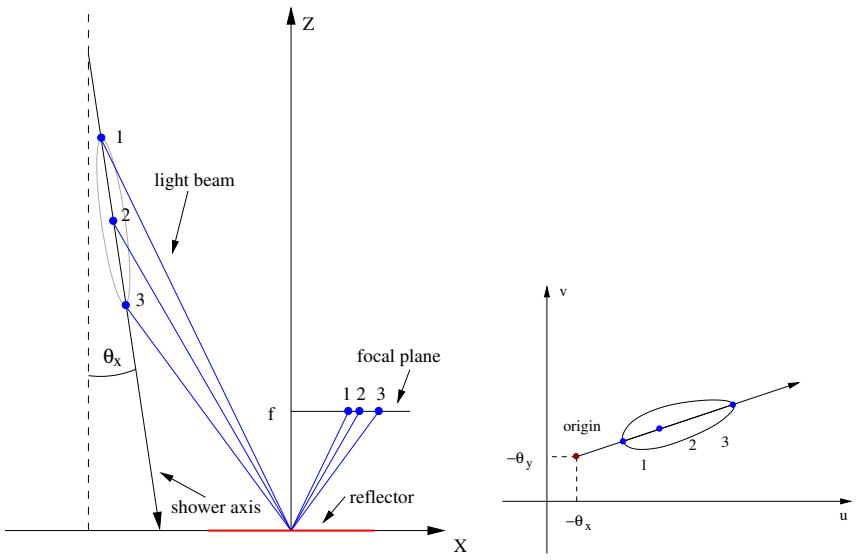

Figure 2.4: *On the left, a schematic illustration of how air showers are depicted in the focal plane is shown. The figure on the right is the camera image as seen from above. Figure taken from [3].*

The camera image of three light emitting points along the shower axis, which is tilted against the z-axis by the angles (θ_x,θ_y), is shown on the right hand side. As can be seen in this sketch, all points along the same angle towards the mirror axis are reflected onto one point on the camera. The equation to calculate the coordinates (u,v) in the camera plane for a focal length f is the following:

$$\begin{pmatrix} u \\ v \end{pmatrix} = -\frac{f}{z} \begin{pmatrix} x \\ y \end{pmatrix} \tag{2.6}$$

This calculation is not linear, leading to a distortion of the camera image. The image of a shower is roughly an ellipse, but the non-linearity stretches it towards the edges and compresses it in the centre of the camera. Nevertheless, the distortion is rather small and most important characteristics of the shower can still be gained from the camera image. The major axis of the ellipsoid, for example, corresponds to the shower axis which points back to the source position. In Section 3.2, the reconstruction method is presented in detail.

The first telescope which ran observations with this technique successfully was a 10-m reflector at the Whipple Observatory. It detected the TeV gamma-ray emission of the Crab Nebula in 1989 for the first time, [1]. Today, all projects on ground-based gamma-ray astronomy use or plan to use a stereoscopic array of IACT telescopes. There are many advantages of adding at least a second telescope:

- If a second image of the same shower, taken from a different direction, is added to Fig. 3.2, the intersection of the shower axes marks the position of the incident photon.

- With stereoscopic viewing a 3D reconstruction is possible, leading to more detailed information about the shower geometry and thus a better discrimination between hadronic and electromagnetic showers.
- the collecting area is increased.
- The energy threshold of the trigger can be lowered, because the discrimination of muons and night sky background (NSB) becomes easier: Usually, the light cone of a muon is too narrow to hit more than one telescope and NSB is a random phenomenon. For this reason a coincidence of multiple telescopes triggering can be required.

As the name High Energy Stereoscopic System indicates, the H.E.S.S. array is one of the gamma-ray telescopes following the stereoscopic approach.

3 The H.E.S.S. Experiment

The High Energy Stereoscopic System (H.E.S.S.) is an array of four telescopes using the Imaging Atmospheric Cherenkov Technique. Its name is a tribute to Victor Hess who discovered cosmic rays in balloon experiments in 1912. Situated at 1800 m above sea level in the dry climate of the Khomas Highland in Namibia, the H.E.S.S. site provides excellent conditions for astronomical observations.

Figure 3.1: *The four telescopes at the H.E.S.S. site.*

In addition to some technical data concerning the telescope system, this chapter will deal with how the observational data taken with H.E.S.S. are analyzed. First, the reconstruction of single events will be presented, then the analysis of whole sources will be introduced briefly. For more detailed information, see [6].

3.1 Telescope system

First observations with H.E.S.S. started in summer 2002 with only one telescope, by December 2003 all four telescopes arranged in a square of 120 m side length were operational. The size of the array is a compromise between stereoscopic viewing, for which large distances are desirable, and a lower trigger threshold that is achieved as long as multiple telescopes are illuminated by one shower.
The telescopes are Davies-Cotton reflectors (described in [7]) in altitude-azimuth (alt-az) mount. Each reflector consists of 382 individual round mirrors of 60 cm diameter, adding up to a total reflector area of 107 m^2. Altogether, they form a hexagon on a spherical surface with a radius equal to the focal length. The camera is located in the focus, at a distance of 15 m. As mentioned above, the camera is required to record few-nanosecond long Cherenkov light flashes. This is provided by using photomultiplier tubes (PMT) as light sensitive elements for each camera pixel plus fast electronics. Possessing 960 pixels with a field of view of 0.16° each, the camera image corresponds to an area of 5° diameter in the sky.
The cameras are not recording constantly, but are triggered by the system electronics if a gamma event may have happened. H.E.S.S. uses a two-step trigger procedure: On the one hand, the image of a single camera must fulfil certain criteria, for example a configurable

amount of pixels has to exceed a minimum of four photo electrons in a time window of 1.5 ns. On the other hand, this applies to all four telescopes and a coincidence with the detection of a possible gamma ray event in at least one of the other cameras must be given.

Observations are done in partitions called "runs", which usually last about 28 minutes each. During one run, the telescopes track a certain object or simply a position in the sky. Different observation modes can be applied allowing different methods of background subtraction:

An object can be observed in ON/OFF-mode, which means that for one run, the targeted source is centred (ON-run) and for the next run, an empty sky field offset by 30 minutes in right ascension, at the same zenith angle is observed (OFF-run). As the OFF-runs contain a similar amount of background as the ON-runs, the difference between them can be taken as a measure for the signal. The disadvantage of the ON/OFF-mode is, that half of the observation time is spent on tracking empty fields.

This drawback does not appear in wobble mode. The source remains in the field of view all the time, but the source position is offset by a certain angle (the off-axis angle) from the pointing direction of the telescopes. In this way, regions outside of the source region are observed at the same time and can be used as background estimates. How this is done exactly will be dealt with in Sec. 3.3.

The precision of the telescope pointing direction is dominated by systematic uncertainties due to misalignments and deformations of the telescope structure, e.g. by wind or gravitation. To keep the errors low, "pointing runs" are conducted regularly. In these runs, a bright star with well-known position is observed with two CCD cameras instead of the regular H.E.S.S. camera. One of the CCD cameras records the star directly while the other one records its reflection in the focal plane. The comparison of the two images allows a detection and correction of pointing errors, therefore the precision for locating sources in the sky is constantly higher than $30''$.

3.2 Event reconstruction

The pictures taken by a telescope are raw camera images, in which an air shower is depicted as an ellipsoid. An example can be seen in Fig. 3.2. The next step is to reconstruct the shower in order to gain information on the event, i.e. the gamma-ray that induced it, particularly the direction it came from and its energy.

The reconstruction technique used to determine the direction and energy of an event is the "Model Analysis" introduced by Mathieu de Naurois and Loic Rolland [8]. It is based on fitting the camera images with calculated shower images from a semi-analytical model. The model includes the precise description of longitudinal, lateral, and angular distributions of charged particles in an air shower. It can be applied to various zenith angles and off-axis angles. In addition, the night-sky background is modelled based on thorough statistical evaluation. Therefore, it does not have to be subtracted and all pixels are considered in the fit.

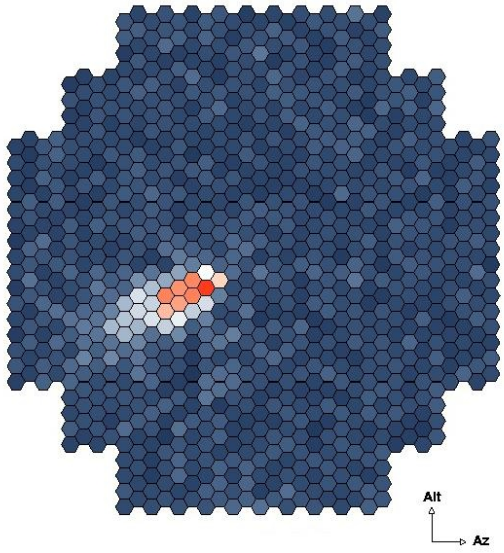

Figure 3.2: *Typical camera image of an electromagnetic shower. Courtesy of K. Bernlöhr.*

In total, there are $\mathcal{O}(10^6)$ simulated shower images for various energies, directions, impact distances from the telescope and first interaction depths, stored in a bank of two-dimensional camera images with very small pixel size. All of them are simulations of showers whose axes equal the telescope axis.

The translation to a real telescope position takes place in the fit procedure since the camera images of the four telescopes are fitted simultaneously. Then, the actual images can be compared to the predicted ones for a given set of primary parameters (energy, direction, impact distance, and first interaction depth). The most likely parameters are found by a log-likelihood fit of the difference in intensity in each pixel between the calculated image and the measured one.

The hadronic background is excluded by a cut on the goodness of fit, called the shower goodness (SG). Showers induced by hadrons are rejected very well as their shapes do not match the calculated images for gamma induced air showers. Several cuts are applied to the camera images in the standard procedure in order to obtain a high quality and reliability:

- The minimum image amplitude is 60 photo electrons per telescope.
- The nominal distance (the distance of the shower center to the camera centre) must not exceed 2°.
- At least the images of two telescopes have to pass the previous cuts to ensure stereoscopic reconstruction.
- A minimal goodness of fit has to be fulfilled, expressed in the shower goodness variable being smaller than 0.6.
- The reconstructed primary interaction depth must be between -1 and 4 X_0.

The resulting energy resolution is better than 15% for the whole energy range (from 80 GeV to 20 TeV) and even better than 10% for the central energy range (500 GeV to 10 TeV). The angular resolution for a single event, defined as 68% of the containment radius, is about 0.06° for zenith angles $< 50°$, it increases to 0.1 for a zenith angle of 70°.

Although the reconstruction reduces different kinds of background events, all gamma-like events are considered. Even for the strongest sources the signal to background ratio is still 1:1, see [9]. Therefore, further steps have to be taken to extract a signal and determine its significance – these will be the topic of the next section.

3.3 Analysis

With only the reconstructed events, it is difficult to discriminate possible sources from background fluctuations. Protons whose showers look like electromagnetic showers and, to a small extent, diffuse gamma rays contribute to the background. As their distribution is rather uniform, it can be assumed that background data taken in a nearby control region approximate the background in a signal region. The strength of the signal can be estimated by the excess parameter N_{excess}, which is the difference between the number of events in the test region (N_{on}) and the control region (N_{off}):

$$N_{\text{excess}} = N_{\text{on}} - \alpha N_{\text{off}} \tag{3.1}$$

By introducing the normalisation constant α, different observation conditions in the control region and in the signal region are taken into account. The obvious differences which may occur are the exposure time and the size of the observed region, but an equally important parameter are variations of the system acceptance $A^{\gamma}_{\text{on,off}}$ between the on- and off-regions. α is the ratio of the system acceptance integrated over the exposure time and angular space of the test region and the background region:

$$\alpha = \frac{\int_{\text{on}} A^{\gamma}_{\text{on}}(\theta_x, \theta_y, \theta_z, t)\, \mathrm{d}\theta_x\, \mathrm{d}\theta_y\, \mathrm{d}\theta_z\, \mathrm{d}t}{\int_{\text{off}} A^{\gamma}_{\text{off}}(\theta_x, \theta_y, \theta_z, t)\, \mathrm{d}\theta_x\, \mathrm{d}\theta_y\, \mathrm{d}\theta_z\, \mathrm{d}t} \tag{3.2}$$

The system acceptance is the probability for a gamma-like event to be reconstructed with a certain energy and position in the field of view after passing the trigger threshold and the above-mentioned analysis cuts. This probability depends on several factors: the reconstructed energy, the distance to the optical axis, the zenith and azimuth angles and the time of the observation. The values $A^{\gamma}_{\text{on,off}}$ have to be determined experimentally, usually they are radially symmetric regarding the observation position.

Having calculated the gamma-ray excess it is still not possible to decide whether there is a source in the tested region or if the signal is the result of background fluctuations. The probability that the measured excess is truly due to a source is expressed by the significance S. It is given in units of the standard deviation of the background, assuming the background fluctuations follow a normal distribution. S can be estimated by the method of Li & Ma [10], which is based on maximum likelihood comparisons:

$$S = \sqrt{2}\left\{ N_{\text{on}} \ln\left[\frac{1+\alpha}{\alpha}\left(\frac{N_{\text{on}}}{N_{\text{on}}+N_{\text{off}}}\right)\right] + N_{\text{off}} \ln\left[(1+\alpha)\left(\frac{N_{\text{off}}}{N_{\text{on}}+N_{\text{off}}}\right)\right]\right\}^{1/2} \tag{3.3}$$

As N_{on} and N_{off} are normally distributed random variables, S is a random variable itself. If there is no source in the tested region, it follows a standard normal distribution.

So far, we simply assumed that N_{off} approximates the background in the on-region. Various techniques concerning the choice of off-regions and the calculation of N_{off} and α exist, for detailed information on the different background subtraction models see [11] . One of them, the Multiple Off Background Model, will be presented because it is used for to estimate the background in the fit algorithm.

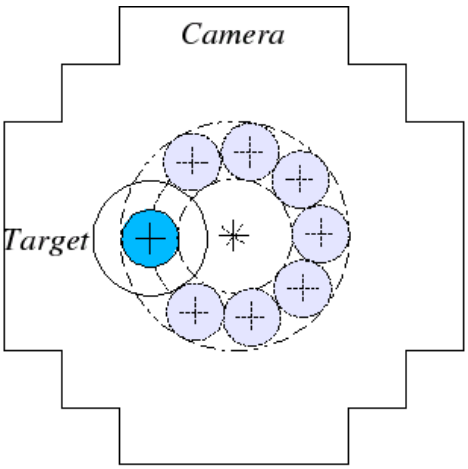

Figure 3.3: *The target region is the blue circle, its radius defined by the θ^2 cut. The second circle around the target is the exclusion region which should not be taken into any off-region calculations as it might be contaminated by gamma-rays from the source. Image courtesy of M. de Naurois.*

The Multiple Off Background Model is applied to runs in wobble mode, i.e. the source position is offset from the observation position by an off-axis angle ϕ. For background estimation, regions of the same size and offset angle as the source region are chosen. Regions containing stars or other gamma-ray sources as well as a circular region around the source are excluded from the background calculations. The number of control regions n_{off} is determined geometrically from the offset angle, the size of the signal region θ^2 and the radius of the exclusion region around the source. As can be seen in Fig. 3.3, they form a ring around the camera axis. Therefore, the acceptance for each of the off-regions is approximately the same as for the on-region and α is simply $\frac{1}{n_{\text{off}}}$.

The reconstructed positions of the events in these regions are all rotated to the source position. This leads to a higher statistic which levels the fluctuations in the background and compensates gradients in different regions. For the same reason, usually runs with different offsets from the source position are chosen and considered together in the background calculation.

In Fig. 3.4, data from the on-region and three rotated off-regions of the Crab Nebula can be seen. The Crab Nebula is the brightest source in the TeV-gamma range, therefore it can easily be recognized and discriminated from the background even without calculating the excess.

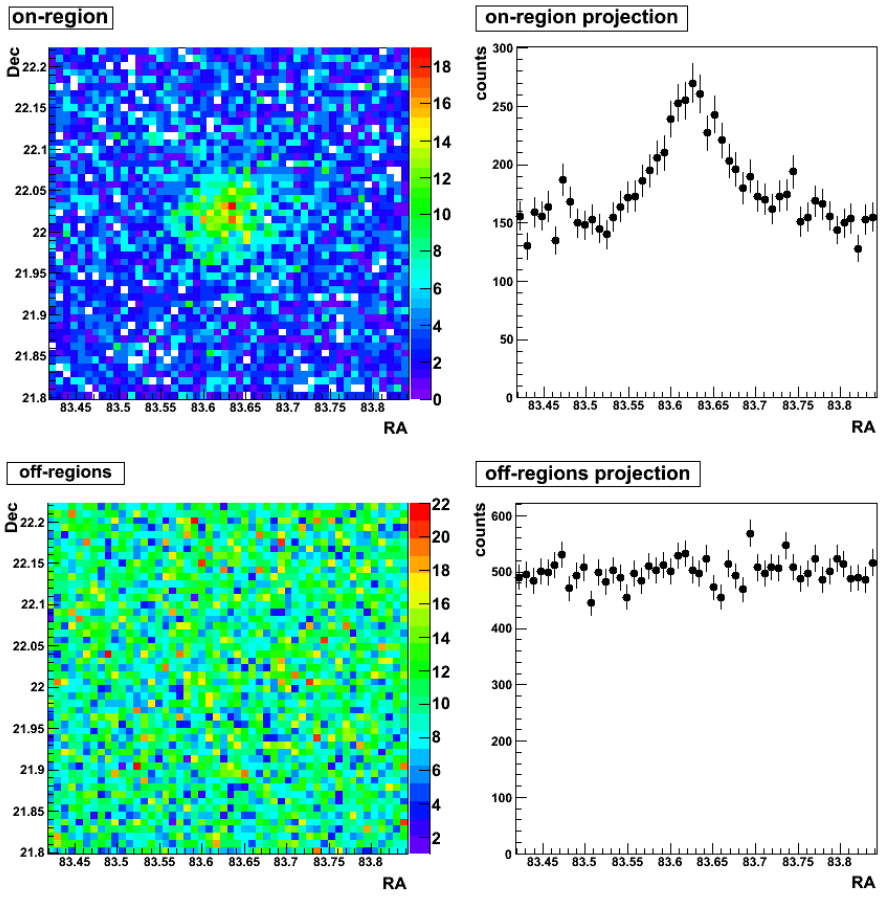

Figure 3.4: *Events of five runs of a Crab Nebula observation. On the upper left the on-region, on the lower left the accumulated data from three off-regions can be seen. The figures on the right are the corresponding projections in the Right Ascension.*

4 The point-spread-function

Every measurement contains not only information about the original source distribution but it is a convolution of the true data with the detector response. Each measured value is blurred due to the uncertainties in the reconstruction. This means that the way we see a source depends on how good the resolution of the detector is, which becomes quite obvious when comparing images of the same source observed with different techniques: The Crab Nebula, as seen in the optical waveband with the Hubble telescope in Fig. 4.1 on the left, is a large structure with many morphological details. In contrast, the same nebula is a point-source for the H.E.S.S. telescope (Fig. 4.1, right picture) because the point spread function (PSF) is much larger. The PSF describes the smearing of a single point, in the case of H.E.S.S. it is measured by the squared angular distance between the reconstructed and the true direction of a Monte-Carlo gamma-ray point-source.

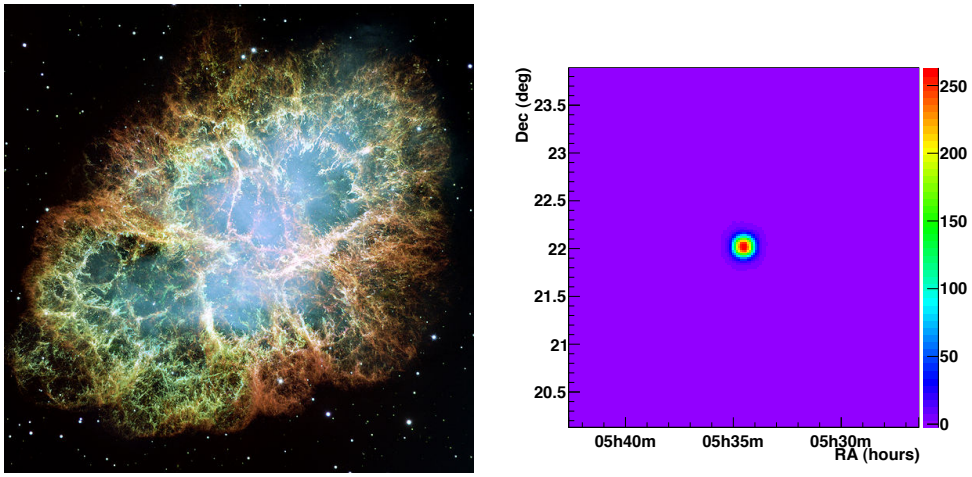

Figure 4.1: *The Crab Nebula as seen with the Hubble Space Telescope (left) and with the H.E.S.S. Telescope (right). The side length of the Hubble image corresponds to about 420′. Credit: NASA/ESA.*

Why is the PSF comparatively large when using IACTs? The essential point is, that IACTs are not observing sources directly but the scattered products of gamma-ray interactions in the atmosphere. These are subject to many statistical processes, for example the depth of the first interaction is randomly distributed. In contrast to the simplified model explained in Sec. 2.1, the number of secondary particles, their energies, and the distances between two interactions are randomly distributed as well. In addition, other processes like Coulomb scattering of electrons take place and change the form of a shower. Therefore, the photon densities measured on ground fluctuate even for gamma-rays with the same energies, as described in [12]. Finally, these photon densities are very low and the collecting area of the telescope system is small in comparison to the “effective” detection area, which is the light pool produced by an air shower on ground.

In general, the PSF depends on the observation conditions, like the zenith angle and the offset, and the reconstruction algorithm applied, especially on the cuts. The aim of this chapter is to determine the characteristics of the H.E.S.S. PSF. This will be done by using Monte Carlo simulations of a point source for various energies, zenith angles, and off-axis angles.

4.1 Model

The Monte Carlo simulations used in this work were produced using KASKADE [13], which is a program simulating the development of air showers. To generate shower images as they would be seen by H.E.S.S., the detection mechanism was simulated in detail, from the geometrical light collection efficiency of the four telescopes to the electronic response of the camera. In this work, simulations of gamma-rays from a point-source detected at 180° azimuth (South) with an optimum camera trigger rate are used. They cover an energy range from 500 GeV to 80 TeV and a zenith angle range from 0° to 70°. The offsets of the simulated observations are 0°–2.5°. An enumeration of all energies, zenith angles and offset angles can be found in Table 4.1. All the simulations are generated in the alt-az system and can be reconstructed with Model Analysis similar to a real point source.

Table 4.1: *Offset angles, energies and zenith angles of the Monte Carlo Simulations which were chosen to study the PSF*

offset angles [°]	0.0	0.5	1.0	1.5	2.0	2.5
energies [TeV]	0.5	0.8	1.25	2.0	3.0	5.0
	8.0	12.5	20.0	30.0	50.0	80.0
zenith angles [°]	0	18	26	32	37	41
	46	50	53	57	69	63
	67	70				

An example of the H.E.S.S. PSF is shown in Fig. 4.2. The data points are projections of a Monte Carlo simulation in the azimuth (left) and zenith (right) direction. This distribution can be described by the sum of two Gaussians (red curve), a narrow one which describes the central peak and a broad one which accounts for badly reconstructed events, see [5]. However, as it has 8 fit parameters (the mean and the variance in two dimensions for two Gaussians) a fit with this description is unstable for low statistics or a high background level. The same curve can be followed by a modified two-dimensional "Student's t-function" $F(x, y)$, which is the black curve in fig. 4.2. The function is described by

$$F(x,y) = \left(1 + \left(\frac{x - m_x}{\sigma_x}\right)^2 + \left(\frac{y - m_y}{\sigma_y}\right)^2\right)^{(-1.5)} . \tag{4.1}$$

With x corresponding to the azimuth and y to the zenith angle, $m_{x,y}$ are the mean values and $\sigma_{x,y}$ define the width of the curve. This leaves only four parameters for the fit and describes the PSF comparatively well: (χ^2), which is a measure for the quality of the fit, is 3482.24 for the double Gaussian and 3466.5 for the Student's t-function, both for a number of degrees of freedom (ndf) of 2500.

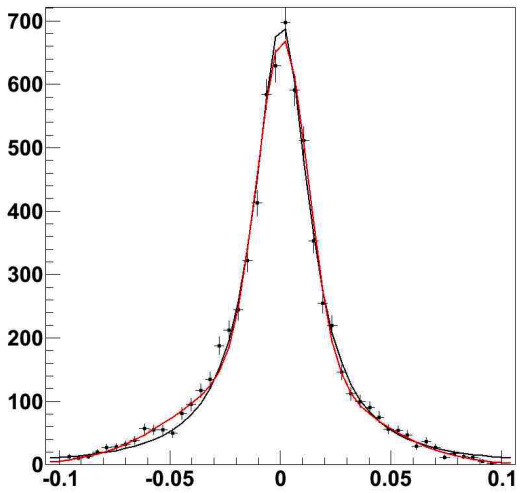

Figure 4.2: *The black data points are a projection of a Monte Carlo Simulation of a point source, observed with an off-axis angle of 0.5° at 41° zenith angle. The simulation contains 3 TeV gamma-rays. The black curve is the fitted modified Student's t-function as in eq. 4.1, the red one is the sum of two Gaussians.*

In the following, Eq. 4.1 is used to describe the form of the PSF.

4.2 Offset, energy and zenith angle dependence

In this section, the dependence of the PSF on the energy and the zenith angle of the incident event as well as on the offset of the observation is examined using the above-mentioned Monte Carlo simulations. All other possible effects, like a dependence on the azimuth, are assumed to be negligible. The characteristics of the PSF are very similar for both directions (altitude and azimuth), therefore only the projections in azimuth direction are depicted in the examples and only the fit values for σ_x are given in comparisons.

There are several factors accounting for the variance of the PSF, a very important one is the shower development through the atmosphere. According to [5], the zenith angle dependency of the PSF is motivated in the following way: At large zenith angles, the first interactions of gamma-rays take place further from the telescope than at small zenith angles. Therefore, also the shower maximum moves away making the image of it smaller. Furthermore, as the Cherenkov light pool broadens, the photon density at ground level is smaller. These effects increase the errors in the reconstruction and broaden the PSF, which can be seen in Fig.4.3: The fitted width of the PSF in azimuth-direction is $(2.48\pm0.03)\times10^{-2}$ deg for a zenith angle of 0°, $(3.72\pm0.06)\times10^{-2}$ deg at 40° and $(4.67\pm0.13)\times10^{-2}$ deg at 57°. All errors given here and later on are 1σ errors, unless otherwise specified.

The energy of the incident gamma ray has a high influence on the formation of the shower as well. The number of Cherenkov photons is directly proportional to the energy of the event, thus the reconstruction errors are smaller for high-energy photons. This is confirmed by the

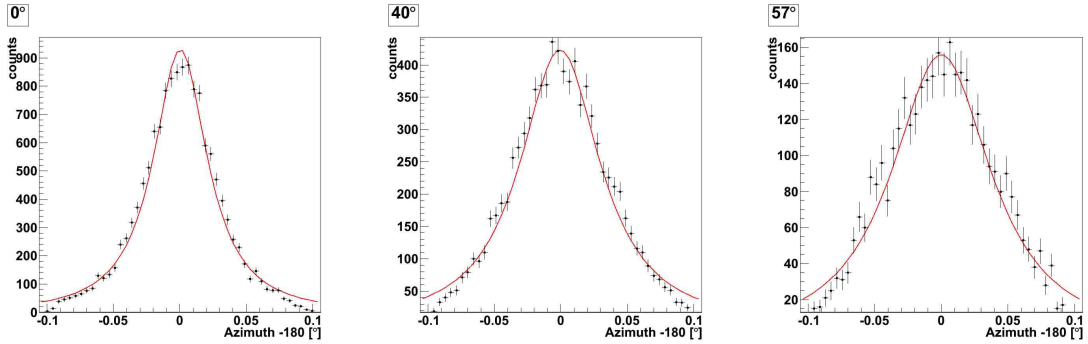

Figure 4.3: *Projections of a simulated point-source (black data points) at 0.8 TeV, observed at an offset of 0.5°, at zenith angles of 0° (left), 40° (middle), and 57° (right) together with the result of the PSF-model as described in the text (red curve).*

fits up to 12.5 TeV, in the left and middle panel of fig. 4.4. For higher energies, the number of simulated events is smaller, which leads to a worse fit of the source as can be seen in the right panel of 4.4. The fitted values of σ_x are $(2.48\pm0.03)\times10^{-2}$ deg, $(2.25\pm0.04)\times10^{-2}$ deg and $(3.28\pm0.3)\times10^{-2}$ deg from left to right.

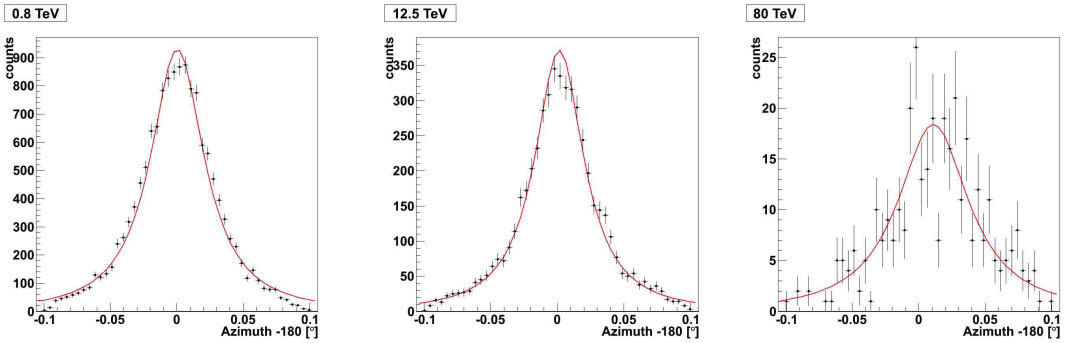

Figure 4.4: *The black data points are projections of a simulated point-source observed with an offset of 0.5° at a zenith angle of 0°, at 0.8 TeV (left), 12.5 TeV (middle), and 80 TeV(right). The red curves are the corresponding PSFs as described in the text.*

Concerning the offset, one would expect the PSF to become broader for bigger off-axis angles as the acceptance of the camera decreases towards its edges. The fits for off-axis angles of 0°, 1.5° and 2.5 ° comply with this expectation, as can be seen in fig. 4.5. σ_x is recorded in histograms with the zenith angle on the x-axis and the logarithm of the reconstructed energy on the y-axis. There are only slight differences between the PSFs for the first two offsets, but for the highest offset the PSF definitely broadens, especially for high zenith angles and energies.

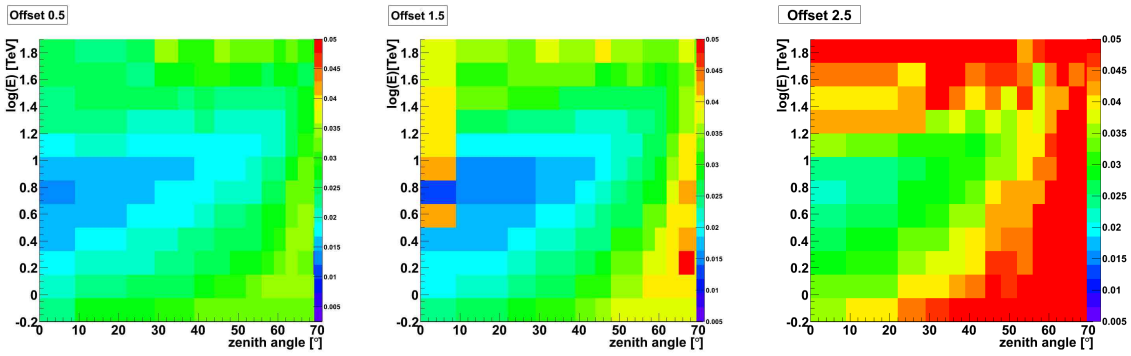

Figure 4.5: *The width of the PSF, σ_x, is color-coded for all zenith angles and energies, for an off-axis angle of 0.5° (left) and 1.5° (right).*

5 The unbinned log-likelihood fit

In the last chapter, we parametrised the functional form of the PSF and found that the width of the PSF depends on the energy and zenith angle of the event and the offset angle of the observation. Thus, the resolution varies for each measured event, but the individual direction errors are not taken into account in H.E.S.S. standard algorithms for the determination of the source position and morphology, see (3.3). In this chapter, the method of unbinned log-likelihood fitting will be presented, which is an approach that considers the variability of the errors. Starting with a brief explanation of the maximum likelihood method, the function used for a fit of the position and extension of a source will be presented and tested.

5.1 The likelihood function

In order to use the unbinned log-likelihood method, the probability density function (pdf) must be defined for all events. In general, every measurement is a random sample from the underlying pdf. The aim is to find this "true distribution" by setting up a model of the pdf, which depends on a set of parameters $\vec{a}$, and maximize the probability of the data to be the outcome of this model.

The pdf of an event $\vec{\xi}$ has to fulfil two conditions: First, it has to be normalised,

$$\int_{-\infty}^{\infty} P(\vec{\xi};\vec{a})\,\mathrm{d}\vec{\xi} = 1. \tag{5.1}$$

Second, the values of the pdf must be positive:

$$P(\vec{\xi};\vec{a}) \geq 0. \tag{5.2}$$

Maximising the pdf by variation of the parameters will give us the highest probability for a given event. As can be derived from Bayes' Theorem, see e.g. [14], the parameters at which the maximum is found are the most probable ones - this is the essential point of the maximum likelihood method. In general, a fit using maximum likelihood means maximising the likelihood function L. For an observation consisting of N events, each with a datum $\vec{\xi}_k$, $k = 0\,..\,N$, the likelihood function is a product of the individual pdfs $P(\vec{\xi}_k;\vec{a})$:

$$L = \prod_{k=1}^{N} P(\vec{\xi}_k;\vec{a}). \tag{5.3}$$

The equation becomes easier to calculate when taking the logarithm: The product is converted into a sum, thus we obtain the log-likelihood function

$$\log L = \sum_{k=1}^{N} \log P(\vec{\xi}_k; \vec{a}). \tag{5.4}$$

As the logarithm is a monotonically increasing function, parameters that will maximise $\log L$ will also maximise L. In words, eq. (5.4) means that the best fitting set of parameters is the one that maximises the sum of the logarithms of the single probabilities.

5.2 The fit function

As mentioned above, the pdf is a model of the observed data and as such must be a description of the signal and the background. In this section, the different terms chosen to fit the data are explained in detail.

The log-likelihood function for fitting a signal without background is

$$\log L = \sum_{k=1}^{N_{\text{sig}}} \log P_{\text{sig}}(\vec{x}_k, E_k, \theta_k, \phi_k; \vec{\mu}, \vec{\sigma}). \tag{5.5}$$

The vector $\vec{x}_k$ denotes the reconstructed x- and y-coordinates of the k-th event in the RA/Dec-System, whereas the fit parameters are the position of the source $\vec{\mu}$ and its extension $\vec{\sigma}$. The signal P_{sig} does not follow the original shape of the source but is a convolution of the source function P_{source} with the PSF, which depends on the energy E_k and the zenith angle θ_k of the event, and the offset ϕ_k, see Chapter 4:

$$P_{\text{sig}} = P_{\text{source}}(\vec{x}_k; \vec{\mu}, \vec{\sigma}) * PSF(E_k, \theta_k, \phi_k). \tag{5.6}$$

For point sources, P_{source} is assumed to be a two-dimensional Gaussian distribution. Tilt angles against the axes are allowed by the inclusion of the fit-parameter ρ, which is 0 if the Gaussian is oriented along the axes and 1 if it is inclined by 45°. The source distribution is then described by

$$P_{\text{source}} = \exp\left(-\frac{1}{2(1-\rho^2)}\left[\left(\frac{x_k-\mu_x}{\sigma_x}\right)^2 + \left(\frac{y_k-\mu_y}{\sigma_y}\right)^2 - \frac{2\rho(x_k-\mu_x)(y_k-\mu_x)}{\sigma_x \sigma y}\right]\right). \tag{5.7}$$

If there is more than one source in the selected area, P_{source} consists of the sum of several Gaussians.

Including background, the fit function is modified to

$$\log L = \sum_{k=1}^{N_{\text{sig}}} \log[(1-f_{\text{bck}})P_{\text{sig}} + f_{\text{bck}}P_{\text{bck}}], \tag{5.8}$$

wherein the fraction of background f_{bck} guarantees the normalisation of the expression. The background is assumed to be the product of polynomials in x and y,

$$P_{\mathrm{bck}}(\vec{x}_k) = P_x(x_k) \cdot P_y(y_k). \tag{5.9}$$

The fit parameters are $f_{x,i}$ and $f_{y,i}$ ($0 \leqslant i \leqslant$ order of the polynomial), the fractions of the different orders of the background polynomials. They increase by two per order, one for x and one for y:

$$P_x = (1 - f_{x,1} - f_{x,2} - ...) \cdot bck_{x,0} + f_{x,1} \cdot bck_{x,1} + f_{x,2} \cdot bck_{x,2} + ..., \tag{5.10}$$

with

$$bck_{x,0} = \frac{1}{n_{x,0}} \quad \text{constant background,}$$

$$bck_{x,1} = \frac{x_k}{n_{x,1}} \quad \text{linear background,}$$

$$bck_{x,2} = \frac{x_k^2}{n_{x,2}} \quad \text{quadratic background}$$

and so on, equivalently for P_y. The denominators $n_{x,i}$ are the normalisation constants for the different orders of P_x.

All the equations so far apply to data taken in an on-region, but as discussed in Sec. 3.3 the discrimination of background noise and events belonging to the signal can be quite difficult and requires the comparison with a matching off-region. In order to determine the background exclusively and with a higher statistic, we can take advantage of the large field of view of H.E.S.S. allowing to find several off-regions with the same acceptance. As explained in Sec. 3.3, they are rotated to the source position, which is convenient since the same fit algorithm and parameters can be applied. The translated coordinates are fitted simultaneously by extending the log-likelihood function with a sum over the total number of events in the off-region, M:

$$\log L = \sum_{k=1}^{N} [(1 - f_{\mathrm{bck}}) P_{\mathrm{sig}} + f_{\mathrm{bck}} P_{\mathrm{bck}}] + \sum_{k=1}^{M} P_{\mathrm{bck}} \tag{5.11}$$

Summarising, the dataset we pass to the pdf consists of the reconstructed shower position, energy, zenith and offset angle. The parameters for the fit are the background fraction f_{bck}, the parameters of the Gaussian source function $\vec{\mu}$, $\vec{\sigma}$,ρ, the background parameters $f_{x,i}$,$f_{y,i}$ and the information if an event is in an on- or off-region. Eq.(5.11) is the function that was finally used for the fit.

The fit is done with MINUIT, [15], a program for function minimization and error analysis developed at CERN, using standard settings except for the error parameter, which has to be set to 0.5 for log-likelihood error estimation. The convolution is performed by Convolution.C (courtesy of S. Heinz, [16]) using the C++ standard library fftw3.

5.3 Test of the fit

Having chosen the method, we have to prove that it is applicable and technically correct. The first step is to simulate data and check if the fit parameters are consistent with and normally distributed around the ones we ran the simulation with.

Assuming that the test source is a true point-source for H.E.S.S., the right function to describe it is a delta-distribution. In that case, the convolution of the source with the PSF is the PSF itself. In order to find deviations in the fitted width, two new parameters a_x and a_y are introduced and multiplied with the widths of the PSF. The indices x and y are corresponding to RA and Dec,respectively. Uniting the scale factors in one vector $\vec{a}$, the pdf for the signal is

$$P_{\text{sig}} = PSF(E_k, \theta_k, \phi_k, \vec{a}). \tag{5.12}$$

Apart from that, the fit function in Eq. 5.11 is used. The background data are random values from a linear distribution which is described by the parameters $f_{x,1}$ and $f_{y,1}$.

As an example, the settings used to obtain simulated data in an on-region and an off-region as shown in Fig. 5.1 are specified. A square with a side length of 0.5° acts as the on-region around the source position at $\vec{\mu} = (10°,10°)$. The background level in the on-region, f_{bck}, is set to 80% . In order to produce a simulated background region, half of the background events are randomly selected to belong to the off-region, which has the same size and position as the on-region. To obtain a higher statistic, seven times the number of background events is generated in the off-region compared to the on-region. Figure 5.1 is a simulation with 500 events, 291 events are depicted in the on-region in the upper left panel and, due to the sevenfold event generation, 1463 events can be found in the off-region.

Except for f_{bck}, the resulting parameters of the fit are all consistent with the values used to run the simulation, as can be seen in Table 5.1. The mean values are fitted with a high precision, but the background parameters are tainted with errors of the same order of magnitude as the values themselves.

Table 5.1: *Comparison of the parameter values used to generate the dataset depicted in Fig. 5.1 and the fitted values.*

parameter	original value	fitted value
$\mu_x[^\circ]$	10.0	10.001 ± 0.003
$\mu_y[^\circ]$	10.0	10.001 ± 0.003
a_x	1.0	0.94 ± 0.14
a_y	1.0	1.03 ± 0.15
$f_{x,1}$	0.2	0.8 ± 0.8
$f_{y,1}$	0.2	-1.4 ± 0.9
f_{bck}	0.8	0.65 ± 0.03

To test the reliability of the fit, 500 samples were simulated and fitted. If the fit works correctly, the fitted parameters p_i^{fit} form a normal distribution with the original value p_i^{true} as its mean and a variance equal to the squared error on the fitted value, e_i. This can be

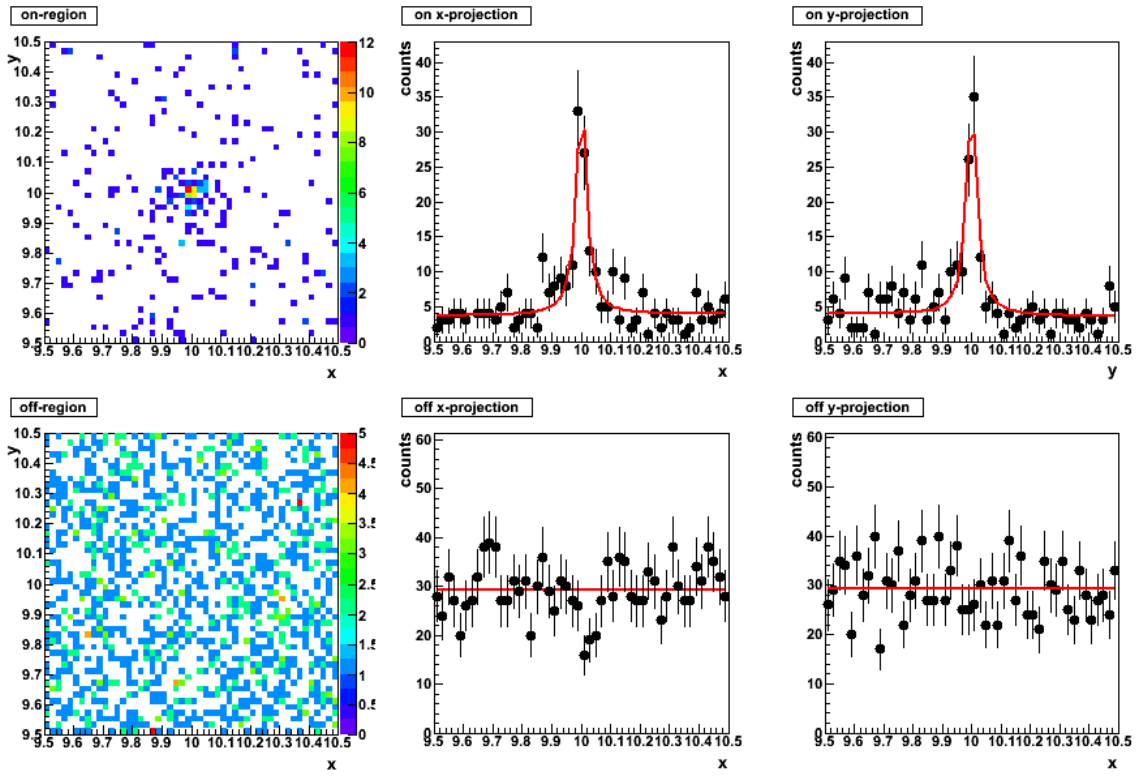

Figure 5.1: *The color-scaled pictures on the left are histograms of a simulated on-region (upper row) and a simulated off-region (lower row) as described in the text. In the middle column, the projections of the simulated data in x-direction are depicted as black points and the red curve is the projection of the fit function. In the column on the right, the projections in y-direction of both data (black) and the fitted curve (red) can be seen.*

checked by generating a so-called "pull-distribution" for each parameter: The values d_i are calculated for each sample according to

$$d_i = \frac{p_i^{fit} - p_i^{true}}{e_i} \tag{5.13}$$

and filled into a histogram. For a large number of samples, the events in this histogram should form a standard normal distribution. The resulting pull-distributions from the 500 fits of the mean $\mu_{x,y}$ and of the extension of the source $\sigma_{x,y}$ conducted for this test can be seen in fig. 5.2.

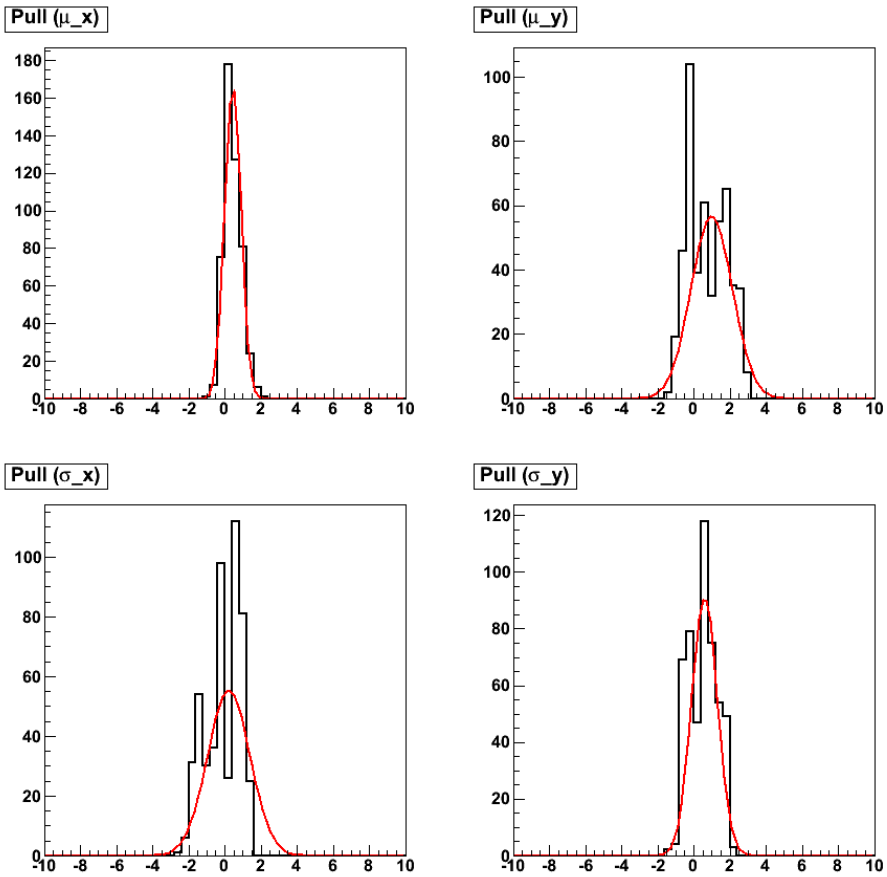

Figure 5.2: *The depicted histograms are the "Pull-distributions" of the parameters μ_x, μ_y, σ_x and σ_y. The red curves are fitted Gaussians, for the result of the fit see Table 5.2.*

The histograms are fitted with Gaussians (red curves), the results of these fits can be seen in table 5.2. The mean values and variances of the Gaussians are not compatible with the expected values within the errors, but as can be seen in Fig. 5.2, a statistic of 500 fitted samples is too low to produce a smooth distribution. Besides of the distribution corresponding to μ_x being too narrow, the shift of the mean values is noticeable.

Table 5.2: *The fitted values of the Gaussians describing the "pull-distributions".*

parameter	mean	variance
μ_x	0.44 ± 0.02	0.46 ± 0.02
μ_y	0.98±0.20	1.14 ± 0.13
σ_x	0.21 ±0.09	1.17 ± 0.06
σ_y	0.59±0.04	0.72 ± 0.02

5.4 Goodness of Fit

The maximum likelihood approach does not indicate any goodness of fit. To state if the chosen model is an appropriate description of the data, a statistical hypothesis test has to be applied. The most commonly used is the χ^2-test, which is applied to data stored in histograms in the following way: If the histogram has N bins, each bin contains a number of entries n_i, $i = 1$ ...N. The number of entries in the corresponding bin which is expected according to the fitted function is denoted as ν_i. The value of interest is X^2,

$$X^2 = \sum_{i=1}^{\mathrm{N}} \frac{(n_i - \nu_i)^2}{\nu_i}. \tag{5.14}$$

Given that the value X^2 follows a χ^2-distribution, it can be used as a measure for the goodness of fit. The distribution depends on the parameter *ndf*, which is the number of degrees of freedom. In this case, *ndf* is the number of bins, N, minus the number of fit parameters, n_p. For large values of *ndf*, the χ^2-distribution converges to a normal distribution. In fig. 5.3, a histogram containing the $\frac{X^2}{ndf}$-values of 200 fits on simulated data mentioned in the last section is shown. Because of the division by *ndf*, a normal distribution with a mean of one is expected - obviously, this does not apply to the values X^2. There are two possible explanations for this result: Either X^2 is not a normally distributed variable and cannot be used as an estimator for the goodness of fit, or the statistics are simply too small.

5.5 Fit of an extended simulated source

The last sections dealt with the fit of a point-source. Since sources detected with H.E.S.S. can be extended or have a more complex morphology, it is desirable to test if the convolution is performed properly and if the algorithm can fit these sources as well. A test is conducted by simulating an extended source with a set of parameter values and comparing them with the fitted ones. The simulated source is a two-dimensional Gaussian with a variance $\sigma_x = 0.2°$ in x and $\sigma_y = 0.05°$ in y. The mean values $vec\mu$ and the background parameter values are chosen as in Sec. 5.3, resulting in simulated data for an on- and off-region as depicted in Fig.5.4 for 5000 events. The parameter values of the fitted function and the values used to generate the data are listed in Table 5.3. The fitted values of $\vec{\mu}$ and $\vec{\sigma}$ match the original ones well within one standard deviation.

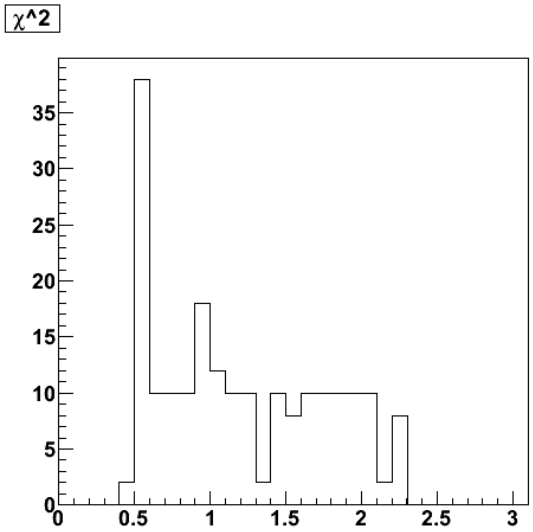

Figure 5.3: *The distribution of the values X^2 for 200 fits on simulated data.*

Table 5.3: *Comparison of the parameter values used to generate the dataset depicted in Fig. 5.4 and the fitted values.*

parameter	original value	fitted value
$\mu_x[^\circ]$	10.0	10.01 ± 0.01
$\mu_y[^\circ]$	10.0	10.015 ± 0.003
$\sigma_x[^\circ]$	0.2	0.197 ± 0.009
$\sigma_y[^\circ]$	0.05	0.054 ± 0.004
$f_{x,1}$	0.2	0.7 ± 0.3
$f_{y,1}$	0.2	0.12 ± 0.3
f_{bck}	0.8	0.67 ± 0.01

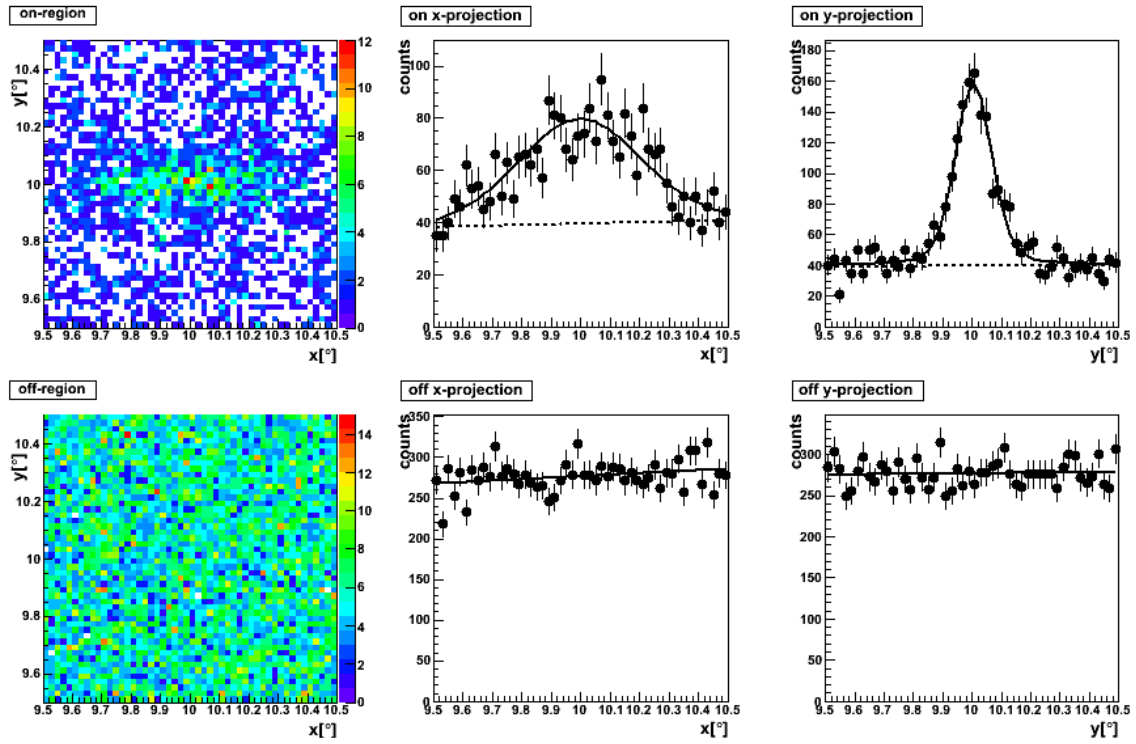

Figure 5.4: *The upper row contains the histograms of a simulation of a signal region (left), the projection of the simulated data in x (middle) and y (right). The black curves are the projections of the fitted function. The lower row contains the corresponding plots for an off-region.*

6 Application to H.E.S.S. data

In this chapter, the unbinned log-likelihood fit will be applied to H.E.S.S. data. First, a test of the PSF on two point-like sources is conducted. According to the results, the sources are fitted with a modified PSF. Finally, the results are compared to the ones of the standard fit procedure of the H.E.S.S. analysis.

6.1 Systematic study of the PSF on point sources

The Monte Carlo simulations described in Chapter 4 are models of an ideal point-source and contain some assumptions. Besides, the Student's t-function might not be a viable choice for the PSF. If the description of the PSF gained from the simulations is correct, the same parameters should be obtained when fitting a real point-source. To verify this, the fit function is modified by introducing scale factors a_x and a_y, as described in Sec. 5.3.

The first point-source on which the PSF is tested is the Crab Nebula, which is the remnant of the 1054 AD supernova explosion and contains the Crab pulsar. As mentioned above, it is the brightest source in the TeV sky and was the first one to be discovered. It is used as a standard candle in gamma-ray astronomy and thus serves as a very well-studied example. Due to the high flux, a small sample of 8 runs is sufficient for a stable fit. The selected runs were taken in November 2004 and December 2005, all with an offset of 0.5°. The coordinates of the nebula are RA 05 h 34 m 32 s, Dec 22° 00' 52" (J2000). Therefore, H.E.S.S. can only detect it at zenith angles $> 45°$, see Fig.6.1 on the left. The energy distribution of the events used in the fit is depicted in the same figure on the right. In order to provide a sufficient amount of background around the source, the size of the on- and off-regions was set to 0.3°. Hence, the number of events is 12936 in the on-region and 35721 in the three off-regions.

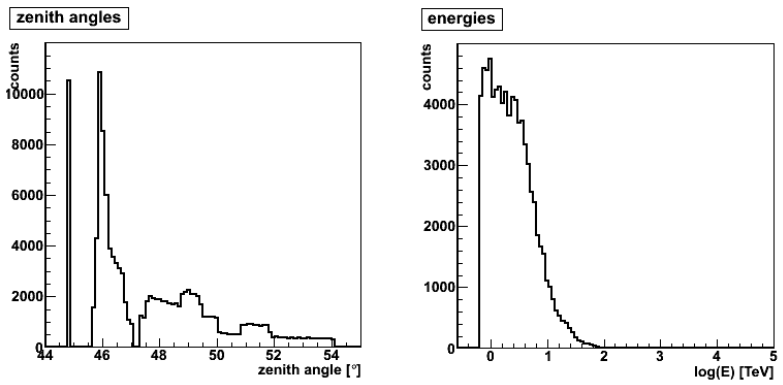

Figure 6.1: *The graphs depict the distribution of zenith angles (left) and of the logarithm of the energies (right) of Crab events from the eight runs used for the fit.*

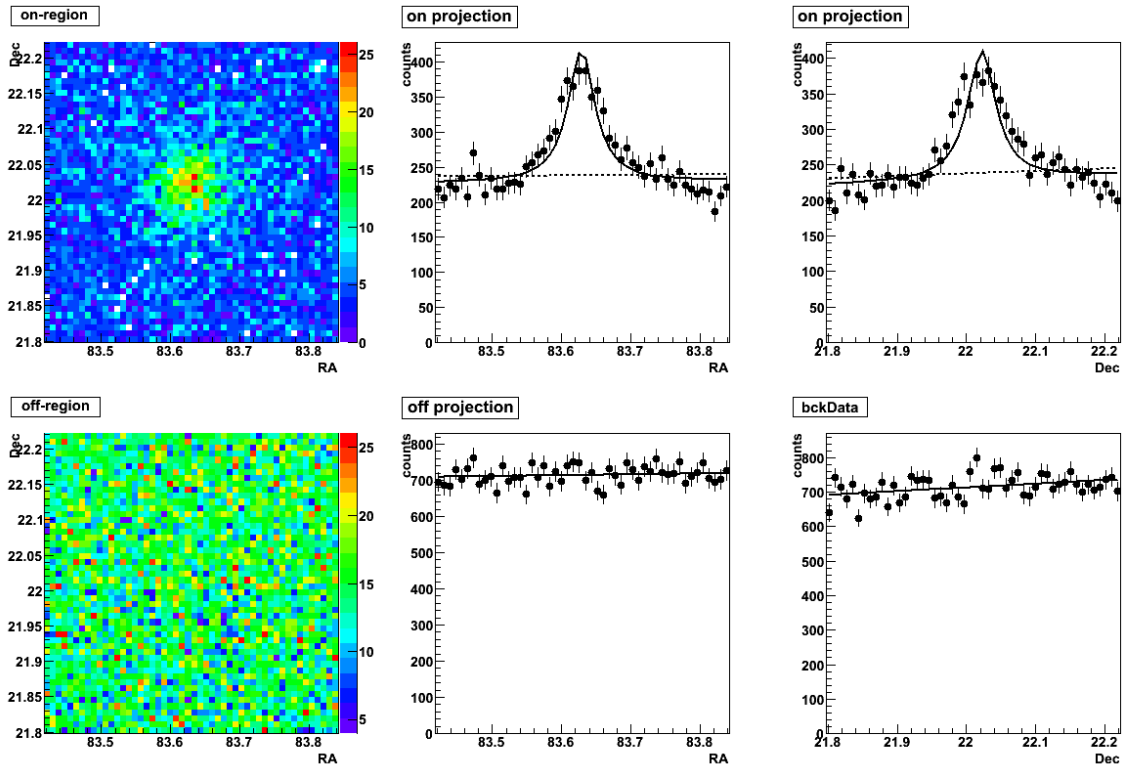

Figure 6.2: *The color-scaled pictures include eight runs of Crab Nebula data. The upper row of images contains the on-data, the lower row the off-data. Black points stand for the data in their projections in RA and Dec, the black curves are the projections of the fitted function (for the parameter values, see Table 6.1). The dotted line in the on-region projections is the fitted background from the off-region divided by the number of off-regions.*

In Fig. 6.2, the data of the Crab Nebula and the fitted function are shown, the fitted parameter values are summarized in Table 6.1. As the position of the source given by the H.E.S.S. standard analysis is RA 86.627°, Dec 22.021°, it is reproduced well by the fit. The scale factors are (0.93±0.05) in RA and (0.98± 0.05) in Dec, which indicates that the PSF is compatible with the data within 2σ. The values of the background parameters $f_{x,1}$, $f_{x,2}$, $f_{y,1}$, $f_{y,2}$ are of the same order of magnitude as their errors, therefore no statement can be made concerning their size. f_{bck}, on the other hand, gives a fair estimate of the background level. Although it could not be proved that the value X^2, defined in Sec. 5.4, is a good estimate of the goodness of fit, it reflects the difference between the fitted function and the data. For the fit of the Crab Nebula, X^2/ndf is 2546.3/2500. The distribution of x_i^2,

$$X^2 = \sum_{i=0}^{\mathrm{N}} x_i^2, \tag{6.1}$$

is depicted in Fig. 6.3.

Table 6.1: *Fit results for a Crab Nebula fit with scale factors.*

parameter	fitted value
μ_x [°]	83.628 ± 0.001
μ_y [°]	22.021 ± 0.001
a_x	0.93 ± 0.05
a_y	0.98 ± 0.05
$f_{x,1}$	1.7 ± 2.8
$f_{y,1}$	1.9 ± 0.9
$f_{x,2}$	0.5 ± 1.3
$f_{y,2}$	0.7 ± 0.4
f_{bck}	0.886 ± 0.005

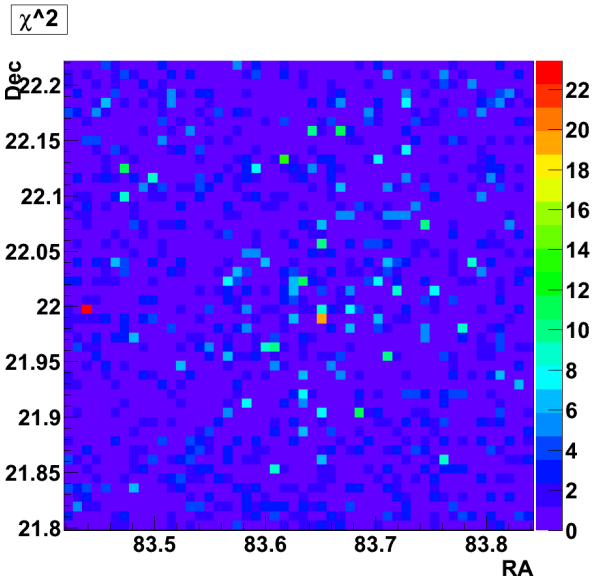

Figure 6.3: *The distribution of x^2 for the fit of the Crab Nebula.*

The second point-source chosen to compare its width with the PSF gained from Monte Carlo Simulations is the Active Galactic Nucleus (AGN) PKS 2155-304. AGNs are extragalactic objects with supermassive black holes accreting matter. They are classified by the visibility of any relativistic jets: PKS 2155-304 is a blazar, i.e. its jet points towards our galaxy and is the source of the emission in the TeV-range. In July 2006, there was a short phase of extreme emission from this source – during the flare, the flux from the blazar increased to almost 100 times its usual flux. Three runs recording the violent outburst were used for the test. Close to 3000 gamma rays were detected in these observations in the on-region with a radius of 0.3°. This is a tremendously high flux considering that the dictance to PKS 2155-304 is 450 Mpc, while the Crab Nebula is as close as 2 kpc. As the equatorial coordinates of this source are RA 21 h 58 m 52 s, Dec -30° 13' 32", it can be observed close to the zenith. The zenith angle distribution and the energy distribution for the three runs are shown in Fig.6.4.

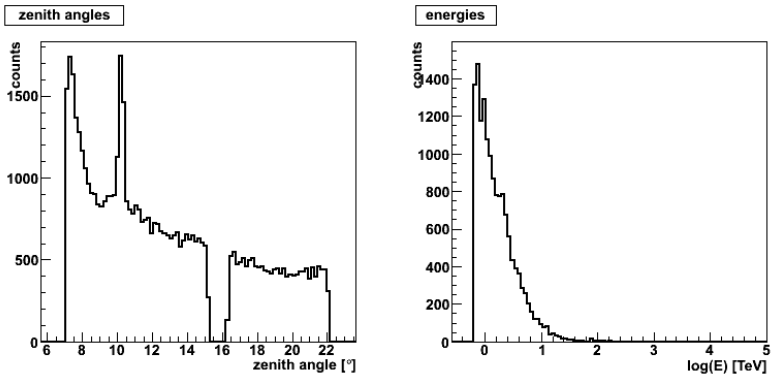

Figure 6.4: *The graph on the left depicts the distribution of zenith angles of the PKS 2155-304 events used in the fit procedure, the graph on the right the distribution of energies on a logarithmic scale.*

Table 6.2: *Fit Results for a PKS 2155-304 fit with scale factors.*

parameter	value
μ_x [°]	329.722 ± 0.001
μ_y [°]	-30.217 ± 0.001
a_x	1.15 ± 0.06
a_y	1.07 ± 0.06
$f_{x,1}$	900 ± 400
$f_{y,1}$	2040 ± 45
$f_{x,2}$	-400 ± 200
$f_{y,2}$	-1020 ± 20
f_{bck}	0.71 ± 0.01

Table 6.2 contains the results of the fit. The scale factors are $a_x = 1.15 \pm 0.06$, and $a_y = 1.07 \pm 0.06$, i.e. the PSF is broader than expected. The fitted position of the source does not match the expected value of RA 329.721°, Dec -30.221° within the error bars, but this may be an effect of only considering the flare runs. The distribution of the squared differences between the true and the fitted values in the single bins, x_i^2, is depicted in Fig. 6.6.

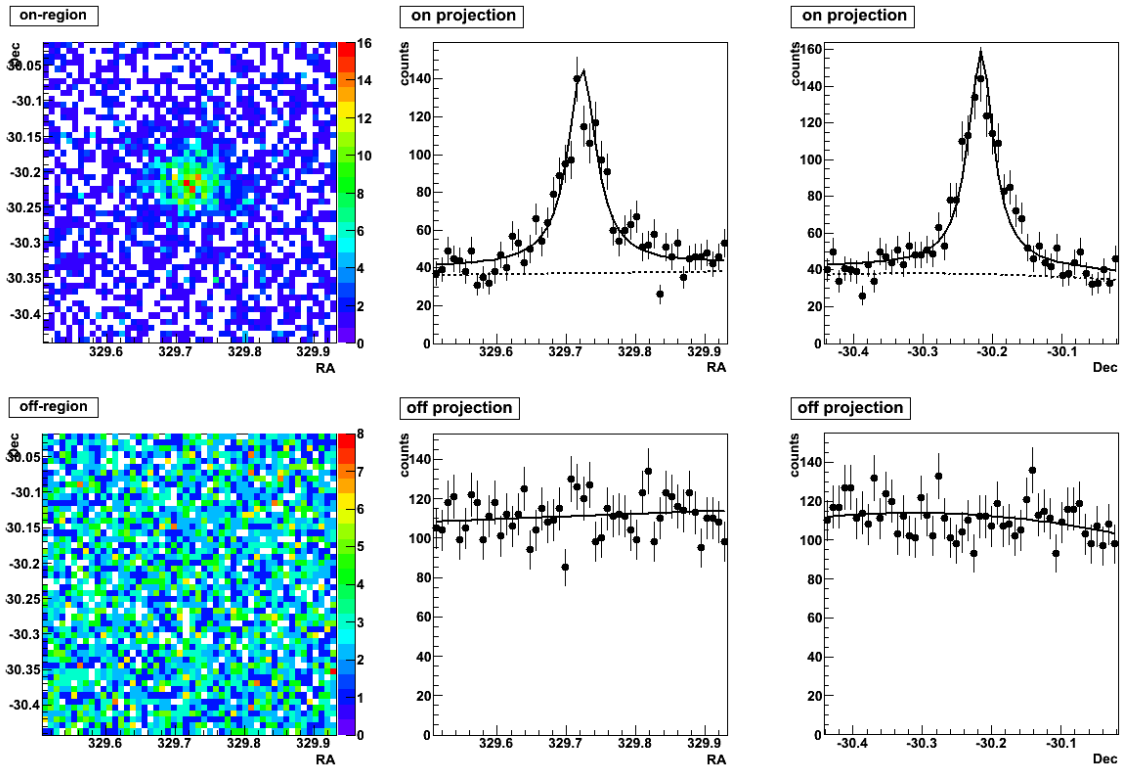

Figure 6.5: *The images in the upper row are, from left to right, a histogram of the on-region, the projection in RA and in Dec (black data-points). The red curves are projections of the fit function with parameters according to Table 6.2. The dotted black curve marks the background function fitted in the off-region, divided by the number of off-regions. In the lower row, the corresponding graphs for the two accumulated off-regions are shown.*

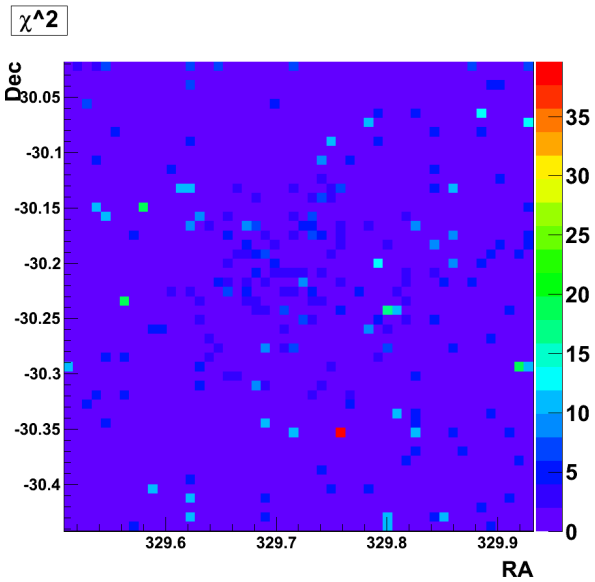

Figure 6.6: *The distribution of x^2 for the fit of PKS 2155-304.*

6.2 Fitting point-sources with a scaled PSF

The scale factors determined in the last section indicate that the PSF is overestimated in the range of zenith angles of the Crab Nebula and underestimated in the range of zenith angles of PKS 2155-304.

Assuming that the Crab Nebula and PKS 2155-304 are not point-sources, the convolution of the source function with the PSF cannot be left out. A fit would show that $\vec{\sigma} \neq \vec{0}$, i.e. the source has an extension. Nevertheless, if the width of the PSF is multiplied with the scale factors derived in the last section, the extension of the source is expected to be consistent with $\vec{\sigma} = \vec{0}$. This check for consistency is accomplished by fitting the two sources with the log-likelihood function as in Eq. 5.11 and scaled PSFs.

The same runs as in the last section are used for the fit of the Crab Nebula. Figure 6.7 shows the result of the fit with a PSF-width multiplied by a_x=0.93 in the right ascension and a_y=0.97 in the declination. As can be seen in Table 6.3, the resulting values for σ_x and σ_y are not matching the expectations: They differ from zero by 8–12 standard deviations.

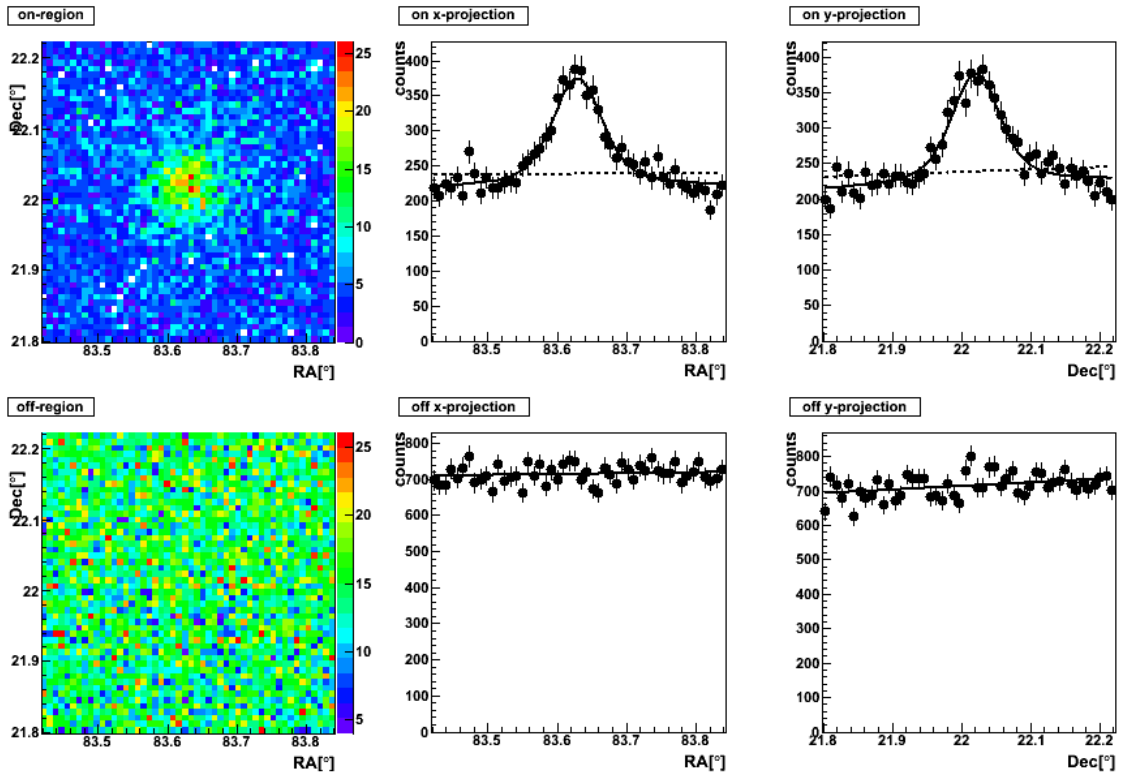

Figure 6.7: *The color-scaled images in the left column as well as the black data-points in the middle and right column are count maps of Crab Nebula data of the signal region (upper row) and the background region (lower row), exactly as in Fig. 6.2. The black curve is the fitted function from the fit with a scaled PSF as described in the text. The dotted line in the projections of the on-region corresponds to the background fitted in the off-region, divided by the number of off-regions.*

In order to confirm that the log-likelihood function reaches a maximum for the fitted parameter values, the behaviour of the function against each parameter is plotted in the vicinity of

Table 6.3: *Parameters of the fit of eight Crab Runs, with a PSF multiplied with the scale factors a_x, a_y from Table 6.1.*

parameter	value
μ_x [°]	83.633 ± 0.001
μ_y [°]	22.025 ± 0.001
σ_x[°]	0.024 ± 0.003
σ_y[°]	0.023 ± 0.002
$f_{x,1}$	1.3 ± 3.2
$f_{y,1}$	1.5 ± 0.8
$f_{x,2}$	0.7 ± 1.6
$f_{y,2}$	0.8 ± 0.4
f_{bck}	0.853 ± 0.006

the maximum. MINUIT is only able to minimize functions and to meet this condition, the sign of $\log L$ is switched. Thus, -$\log L$ is plotted versus μ_x, μ_y, σ_x and σ_y in Fig. 6.8.

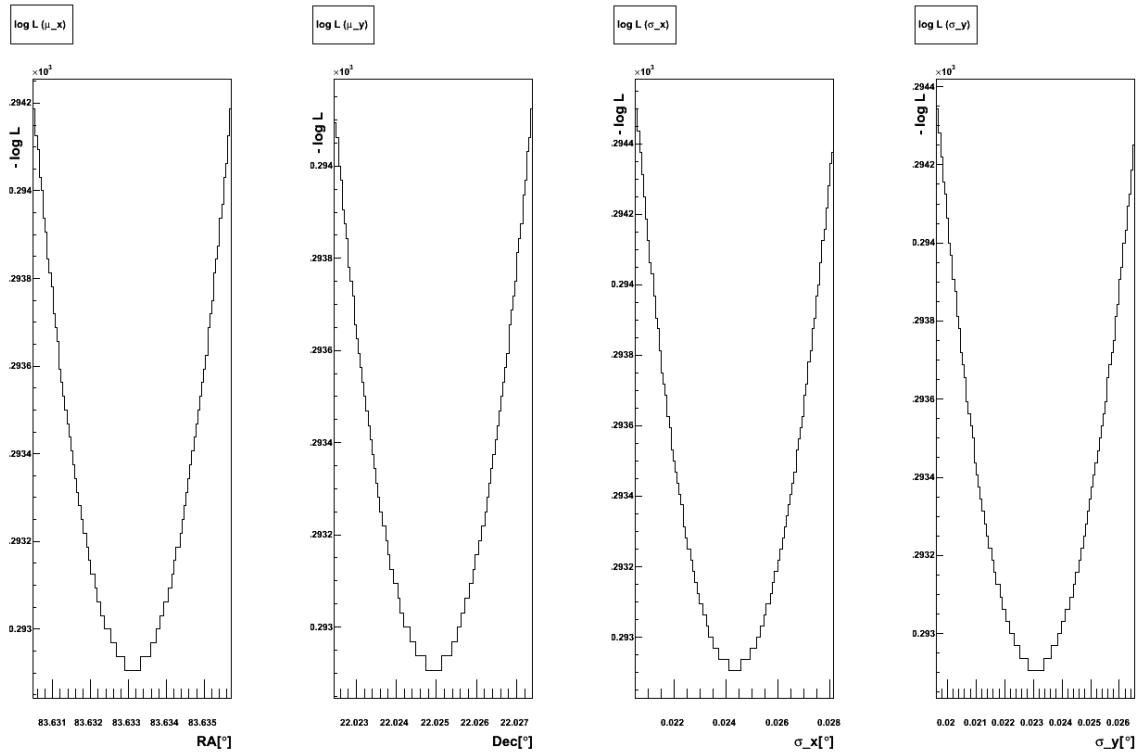

Figure 6.8: *The graphs visualize the dependence of the fit function (-$\log L$) on the parameters μ_x, μ_y, σ_x and σ_y, from left to right, in the vicinity of the fitted minimum for the Crab Nebula.*

For PKS 2155-304, the test was applied on the three flare runs which were already used in the fit without convolution. Figure 6.9 contains the on- and off-data of these runs as well as the projections of the functions fitted with a PSF scaled with a_x=1.15 in RA and a_y=1.07 in Dec. The fitted parameters are listed in Table 6.4. The values for σ_x and σ_y are again

inconsistent with the expectation as they predict an extension of (0.021±0.003)° in RA and (0.016±0.002)° in Dec. Again, the negative log-likelihood function -log L is plotted against each parameter to show that the maximum is found at the fitted parameter values, see **??**.

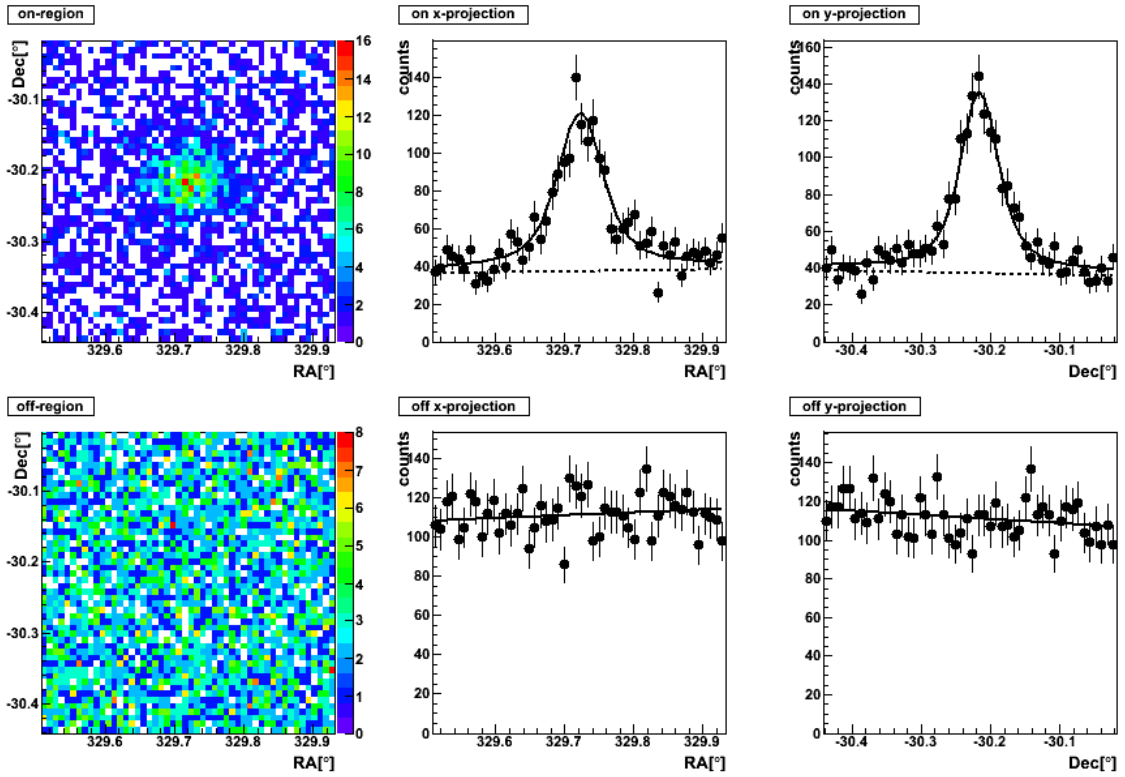

Figure 6.9: *The histograms depicted in the upper row contain on-region data of PKS2155-304. The histogram on the left is a count map of the reconstructed events, the histograms in the middle and on the right are its projections in RA and Dec, respectively. The lower row shows the corresponding histograms for the off-region. The fitted function is shown as black curve, the dotted line in the on-data projections is the normalized level of background fitted in the off-region.*

Table 6.4: *Parameters of the fit on PKS 2155-304, with a PSF multiplied with the scale factors a_x, a_y from Table 6.2*

parameter	value
μ_x [°]	329.726 ± 0.002
μ_y [°]	-30.212 ± 0.001
σ_x[°]	0.021 ± 0.003
σ_y[°]	0.016 ± 0.002
$f_{x,1}$	21 ± 492
$f_{y,1}$	3 ± 45
$f_{x,2}$	11 ± 246
$f_{y,2}$	1 ± 22
f_{bck}	0.67 ± 0.01

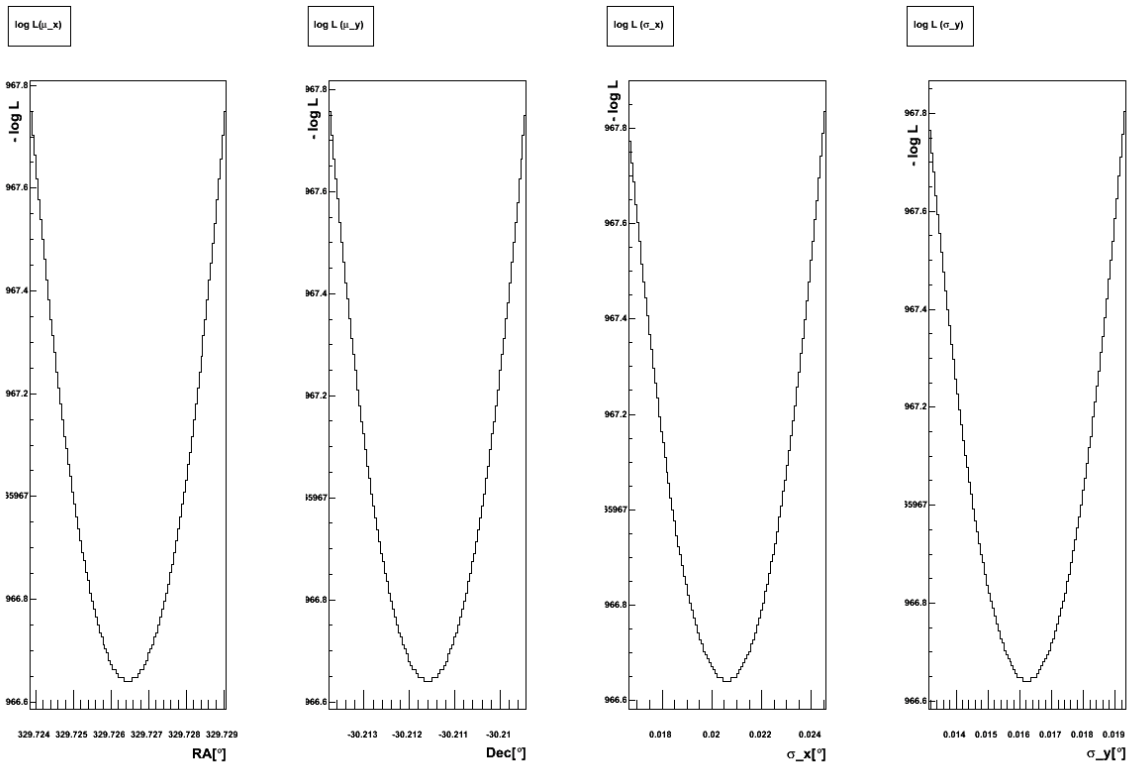

Figure 6.10: *These graphs visualize the dependence of the fit function (*-log L*) on the parameters* μ_x*,* μ_y*,* σ_x *and* σ_y*, from left to right, in the vicinity of the fitted minimum for PKS 2155-304.*

6.3 Comparison with the standard analysis fit

Subsequent to the analysis described in Sec. 3.3, source positions and morphologies of analysed signals can be fitted with the log-likelihood method as well. In opposite to the fit procedure presented in this work, the standard fit is applied to binned data. Its basic principle are comparisons of the distribution of measured data with an expected morphology. The possible morphologies implemented in the fit correspond to point-sources, Gaussian-shaped extended sources or even ring sources.

Point-like sources are fitted with a two-dimensional delta function. The position of the Crab Nebula, determined by analysing all 125 observation runs of it with this method, is RA 83.6273±0.0003, Dec 22.0213±0.0003. The errors of the standard fit are about one third of the errors on the position in the unbinned log-likelihood fit.

The same applies to the 600 analysed runs of PKS 2155-304: The fitted values of its position in the equatorial coordinate system are RA 329.7210±0.0002, Dec -30.2215±0.0002, while the values fitted in Sec. 6.2 are RA 329.726±0.002, Dec -30.212±0.001 .

It has to be kept in mind, that the unbinned log-likelihood fit was applied to only eight observation runs of the Crab Nebula, and only three runs of PKS 2155-304. For a significant comparison of the two methods, the same number of runs must be analysed and fitted.

7 Conclusions and outlook

In this work, the H.E.S.S. PSF has been parametrized and used to set up an unbinned log-likelihood fit for gamma-ray sources. The fit algorithm was tested on simulated sources and applied to two real point-sources. It could be shown that the unbinned log-likelihood fit is a viable method to locate source positions as both, simulated and real data, are fitted well and with a high precision.

Although fits on simulated sources show a good agreement, there are inconsistencies concerning the fit of real source extensions. Fitting point sources with a scaled PSF as described in Sec. 6.2 should result in a spacial extent compatible with zero. Nevertheless, the fitted widths of both tested sources do not meet this requirement. This may have various reasons: On the one hand, the effects of binning, which is required for the convolution, are insufficiently studied. The convolved source function is stored in histograms with a bin size corresponding to 0.01°, this is about half of the fitted "extension" of a point source and may affect the resolution. On the other hand, the description and parametrization of the PSF are improvable. A better understanding of the PSF and its dependencies is crucial for the success of the method. A first step would be to study the dependency on the azimuth angle, as the PSF changes depending on the angle to the Earth's magnetic field. In addition, there statistical validity of the fit algorithm is still to be verified.

Having successfully fitted simulated sources with an extension, it is reasonable to assume that the method is also applicable to real extended sources. When this is accomplished, the next step would be to fit sources with complex morphologies. Another interesting direction for further investigation is in how far the method might be used for the discrimination of neighbouring sources.

Summarizing, a lot of work still has to be done, but the unbinned log-likelihood method shows good prospects for further developments.

Bibliography

[1] T. C. Weekes, M. F. Cawley, D. J. Fegan, K. G. Gibbs, A. M. Hillas, P. W. Kowk, R. C. Lamb, D. A. Lewis, D. Macomb, N. A. Porter, P. T. Reynolds, and G. Vacanti. Observation of TeV gamma rays from the Crab nebula using the atmospheric Cerenkov imaging technique. *apj*, 342:379–395, July 1989.

[2] Scott Wakely and Deirdre Horan. http://tevcat.uchicago.edu/.

[3] Julia Brucker. Investigation of h.e.s.s. skymaps by means of minkowski functionals. *Diploma Thesis*, 2007.

[4] W. Heitler. Quantum theory of radiation, 3rd edn. (dover press). 1954.

[5] David Berge. A detailed study of the gamma-ray supernova remnant rx j1713.7-3946 with h.e.s.s., 2006.

[6] Aharonian et al. Calibration of cameras of the h.e.s.s. detector. *Astroparticle Physics*, 22(2):109 – 125, 2004.

[7] John M. Davies and Eugene S. Cotton. Design of the quartermaster solar furnace. *Solar Energy*, 1(2-3):16 – 22, 1957. The Proceedings of the Solar Furnace Symposium.

[8] Mathieu de Naurois and Loic Rolland. A high performance likelihood reconstruction of gamma-rays for imaging atmospheric cherenkov telescopes. *Astroparticle Physics*, 32(5):231 – 252, 2009.

[9] Aharonian et al.

[10] T.-P. Li and Y.-Q. Ma. Analysis methods for results in gamma-ray astronomy. *apj*, 272:317–324, September 1983.

[11] D. Berge, S. Funk, and J. Hinton. Background modelling in very-high-energy gamma-ray astronomy. *A&A*, 466(3):1219–1229, 2007.

[12] V. R. Chitnis and P. N. Bhat. Cerenkov photon density fluctuations in extensive air showers. *Astroparticle Physics*, 9(1):45 – 63, 1998.

[13] M. P. Ketzman and G. H. Sembroski. Nucl. instrum. meth. a. 1994.

[14] Glen Cowan. Statistical data analysis. pages 2–3, 1998.

[15] Minuit homepage.

[16] Sebastian Heinz. Studien zu entfaltungsmethoden f́ur die verbesserung der morphologischen aufĺosung von h.e.s.s. quellen. *Diploma Thesis*, 2008.

Danksagung

Viele Menschen haben zum Gelingen dieser Diplomarbeit beigetragen, sowohl durch fachlichen Rat als auch durch Unterstützung in anderen Belangen. Einigen von Ihnen möchte ich an dieser Stelle besonders danken.

Allen voran gilt mein Dank Christian Stegmann, der mir die Möglichkeit gegeben hat mich mit dem spannenden Gebiet der Gammastrahlungsastronomie zu beschäftigen. Für die gute Betreuung, die fachliche Hilfe und die vielen Stunden die er mir geopfert hat, aber auch - und nicht weniger - für die Offenheit und die angenehme Arbeitsatmosphäre, für die interessanten Gespräche und kleinen Aufmunterungen.

Viel zu verdanken habe ich der ganzen H.E.S.S.-Gruppe in Erlangen, die neben wissenschaftlichen Hilfestellungen für allseits geliebte Kaffeepausen gesorgt hat. Hervorheben möchte ich an dieser Stelle Daniel, der mir die Arbeit mit einigen genialen Einfällen deutlich erleichtert hat, und das gesamte Zimmer 312 - Constanze, Julia und Arnim hatten immer ein offenes Ohr und eine Menge guter Tipps parat. Sebastian möchte ich für die Betreuung in den ersten Monaten danken, für die vielen Erklärungen und nicht zuletzt für den Faltungsalgorithmus, den ich in meiner Arbeit verwendet habe.

Der Austausch mit Markus, Michi und Neli hat mich sehr oft weitergebracht, obwohl - oder vielleicht gerade weil - wir an sehr unterschiedlichen Themen gearbeitet haben. Neli möchte ich noch einmal ganz besonders danken, weil sie als echte Freundin jederzeit für mich da war. Genauso bedanke ich mich bei Luzi, mit der ich über alles reden konnte und viel Spass hatte, und Felix, der die Quitten für das gemeinsame Gelee-Kochen geerntet und große Teile meiner Arbeit korrekturgelesen hat. Wichtig sind an dieser Stelle auch Maria und Johannes, die mir trotz der großen und wechselnden Distanzen immer sehr nahe geblieben sind.

Meinen Eltern und meiner Schwester möchte ich für den Rückhalt, die Gedanken die sie sich um mich machen und die vielen Telefonate danken.

Als Letzter auf dem Papier, in Gedanken immer der Erste, ist Matthias.

Persönliche Erklärung

Hiermit erkläre ich, dass ich diese Arbeit selbstständig angefertigt und keine anderen als die angegebenen Hilfsmittel verwendet habe.

Erlangen, den 11. November 2010

Kornelia Stycz